Water Air Soil Pollut (2026) 237:169
https://doi.org/10.1007/s11270-025-08868-1

Exploring CuO/Nano Graphitic Carbon Nitride Composites as Photocathode in Photocatalytic Fuel Cells

Kang-Zheng Khor · Soon-An Ong · Nabilah Aminah Lutpi · Yunhai Wang · Jai-Xien OrYang · Li-Ngee Ho

Received: 22 August 2025 / Accepted: 12 November 2025

Abstract Photocatalytic fuel cells (PFCs) offer a sustainable approach to energy conversion from organic pollutants, but their efficiency is often hindered by the cathode, which has a slow oxygen reduction reaction (ORR) and limits the transportation of electrons to the cathode from the photoanode. In this study, CuO/nano g-C_3N_4 composites with different CuO ratios were synthesized and loaded onto carbon plates as cathodes to enhance ORR activity for Reactive Red 120 (RR120) degradation and generation of electricity in the PFC system. The synthesized nano g-C_3N_4 and its composites were characterized with Fourier transform infrared spectroscopy (FTIR), X-ray diffraction (XRD), X-ray photoelectron spectroscopy (XPS), UV–Vis diffuse reflectance spectroscopy (UV–Vis DRS), nitrogen adsorption–desorption analysis and field emission scanning electron microscopy (FE-SEM). The results disclosed that the application of CuO/nano g-C_3N_4 as the cathode under dual photoelectrode configuration promoted charge separation and facilitated electron transfer and achieved optimal PFC performance, with a 98.46% removal efficiency and maximum power density (P_{max}), 1.351 mW/m^2, which was 167.15% higher than the pristine nano g-C_3N_4. These discoveries highlighted the potential of CuO-modified nano g-C_3N_4 composites in improving ORR efficiency and generating electricity.

Highlights

- Incorporating CuO into nano-g-C_3N_4 improved the maximum power output and organic pollutant degradation efficiency.
- The highest CuO-to-nano g-C_3N_4 ratio did not lead to improved electricity generation performance in the PFC system.
- The dual-photoelectrode configuration significantly enhanced the overall performance of the PFC system.
- The kinetic rate constant for dye degradation was influenced by the band gap of the electrocatalyst.

Keywords Photocatalytic fuel cell · CuO/nano g-C_3N_4 composites · Cathodic catalyst · Wastewater treatment · Electricity generation · Degradation

Supplementary Information The online version contains supplementary material available at https://doi.org/10.1007/s11270-025-08868-1.

K.-Z. Khor · J.-X. OrYang · L.-N. Ho (✉)
Faculty of Chemical Engineering & Technology, Universiti Malaysia Perlis (UniMAP), Perlis, Malaysia
e-mail: holingee@yahoo.com; lnho@unimap.edu.my

S.-A. Ong · N. A. Lutpi
Water Research and Environmental Sustainability Growth, Centre of Excellence (WAREG), Faculty of Civil Engineering & Technology, Universiti Malaysia Perlis (UniMAP), Perlis, Malaysia

Y. Wang
Department of Environmental Science and Engineering, Xi'an Jiaotong University, Xi'an 710049, China

Published online: 22 November 2025

1 Introduction

In recent years, growing technological advancements and global concerns about environmental disruption and energy resources have driven significant attention toward clean and sustainable energy technologies like photocatalytic fuel cells (PFCs) due to their eco-friendly nature, high efficiency, and ease of operation. In PFCs, the overall system performance is greatly influenced by several factors, including the photocatalytic activity of the photoanode, radical reactions in the solution, and the cathode reaction, oxygen reduction reaction (ORR) (Ong et al., 2021). The efficient performance of energy conversion systems such as fuel cell technologies heavily relies on the ORR, a crucial electrochemical process at the cathode. Electrocatalysts, or cathodic catalysts, and their surface science are vital components that directly influence the ORR kinetics (Bentley et al., 2019; Liu et al., 2020). The ORR at the cathode governs the consumption of electrons in the PFC, which directly impacts the generation of photogenerated holes at the photoanode, power output, and their associated oxidation reactions (Lee et al., 2018; Ong et al., 2021). However, at the cathode, the sluggish kinetics of the ORR, which is significantly slower than the electron generation rate at the photoanode, often lead to substantial energy losses and hinder the overall performance of these systems (Alemany-Molina et al., 2022; Li et al., 2024). Thus, enhancing ORR efficiency at the cathode is a critical pathway to improving PFC performance, which necessitates the development of advanced cathodic catalysts that can accelerate ORR while ensuring high stability and cost-effectiveness for efficient energy conversion technologies. Currently, platinum-based catalysts are the most widely used cathode materials due to their high ORR activity (Madima & Raphulu, 2025; Ouyang et al., 2022). Nonetheless, their high cost and limited availability make them impractical for large-scale applications, highlighting the need for alternative, cost-effective catalysts such as graphitic carbon nitride (g-C_3N_4) and copper oxide (CuO), which is a transition metal oxide with a positive redox potential in the electrochemical series, as platinum, can promote oxygen activation and electron transfer in ORR, making it a promising candidate as a cathodic catalyst.

Graphitic carbon nitride (g-C_3N_4) is a potential photocatalyst because of its unique structural and electronic properties, including a tunable bandgap, high thermal stability, and excellent chemical robustness. Additionally, its two-dimensional structure with abundant surface-active sites makes it highly attractive for photocatalytic applications (Li et al., 2021; Taghipour et al., 2022). Despite these advantages, the limited conductivity, inadequate light utilization and rapid recombination of charge carriers by photogeneration in pristine g-C_3N_4 hinder its catalytic performance, particularly in ORR (Anjumol et al., 2023). Modifying pure g-C_3N_4 with transition metal oxides, including CuO, has become a viable strategy to get beyond its drawbacks. CuO, a semiconductor (p-type) with a narrow bandgap (1.2 eV) and excellent redox activity, is a highly efficient ORR/OER catalyst due to its electron-accepting properties, which enhance charge separation and thereby enhance the overall photocatalytic performance of the composite (Kum et al., 2013). Additionally, CuO offers favorable electrochemical properties, environmental friendliness, and strong oxygen reduction catalytic ability for oxygen reduction (Shang et al., 2022; Yap et al., 2021). The synergy between nano g-C_3N_4 and CuO is believed to not only facilitate ORR kinetics but also broaden the light absorption range, making the composite an ideal candidate as the cathodic catalyst in PFCs.

The most recent studies have explored g-C_3N_4-based materials for various applications in electrochemical, including their use as photocatalysts, electrocatalysts, and photoanodes in photoelectrochemical cells for hydrogen production, as well as in PFCs for environmental remediation and energy recovery (Arulkumar et al., 2024; Qiao et al., 2024; Wu et al., 2023). However, despite its potential, research on using CuO-g-C_3N_4 composites as a cathodic catalyst in PFCs remains largely unexplored. Based on our understanding and knowledge, the studies concerned on utilizing CuO/nano g-C_3N_4 composites specifically as cathodic catalysts in PFC systems. Exploring this underutilized aspect could unlock new possibilities for enhancing PFC performance by leveraging g-C_3N_4's photocatalytic capabilities for ORR. This gap in research highlights the novelty and importance of the current study. In this work, we attempted to evaluate and compare the CuO/nano g-C_3N_4 composites as cathodic catalysts on the carbon plate for PFCs under single and dual photoelectrodes configuration, respectively. It is worth pointing out that this is the

first time that CuO/nano g-C_3N_4 composites have been used as a photocathode, which was coated on a carbon (C) plate in the PFC system. By investigating the complementary properties of CuO and nano g-C_3N_4, the study seeks to address the critical challenges in ORR and provide a sustainable and efficient alternative resolution to improve the performance of PFC systems.

2 Experimental Details

2.1 Chemicals

Reactive Red 120 (RR120) ($C_{44}H_{30}Cl_2N_{14}O_{20}S_6$), from Sigma Aldrich (St. Louis, MO, USA), was used as the pollutant. A 95% purity of ethanol, C_2H_5OH, and ethylene glycol, $(CH_2OH)_2$, from HmbG Chemicals, were used in this research. Copper (II) acetate, $C_4H_6CuO_4 \bullet H_2O$ (R&M Chemicals), melamine, with the molecular formula, $C_3H_6N_6$, supplied by Sigma Aldrich (St. Louis, MO, USA), and zinc (II) oxide, ZnO, from HmbG Chemicals, were used in the cathodic catalyst synthesis and photocatalyst, respectively. The chemicals used were scientific grade.

2.2 Nano Graphitic Carbon Nitride (Nano g-C_3N_4) Synthesis

The synthesis method of nano g-C_3N_4 was modified from the procedure outlined by Madankar et al. (2025). The nano g-C_3N_4 was synthesized by calcining melamine to 580 °C for 4 h with a 10 °C/min heating rate. Then, the synthesized nano g-C_3N_4 composite was cooled to room temperature and ground into powder.

2.3 CuO/nano g-C_3N_4 Composites Synthesis

CuO/nano g-C_3N_4 composites were synthesized by calcining $C_4H_6CuO_4 \bullet H_2O$ and $C_3H_6N_6$ under controlled conditions in a muffle furnace. Firstly, the CuO/nano g-C_3N_4 composites with varied compositions were prepared with a mass ratio of $C_4H_6CuO_4 \bullet H_2O$:$C_3H_6N_6$ in 0.5:9.5, 1:9, and 2:8, and labelled as Cu0.5GCN9.5, Cu1GCN9, and Cu2GCN8, respectively. $C_4H_6CuO_4 \bullet H_2O$ and $C_3H_6N_6$ were mixed well, then heated up to 580 °C for 4 h with a 10 °C/min heating rate. Finally, the synthesized CuO/nano g-C_3N_4 composite was cooled to room temperature and ground into a powder.

2.4 Preparation of Electrodes

The electrodes were divided into cathode and anode. The cathodes included the nano g-C_3N_4/C, Cu0.5GCN9.5/C, Cu1GCN9/C, and Cu2GCN8/C, and an anode of ZnO/C was prepared using the immobilization method. Carbon plates with dimensions of 5.00 cm × 3.00 cm × 0.30 cm were used as the substrate of the electrodes. Firstly, the carbon plates were cleaned thoroughly by ultrasonic cleaning in distilled water and ethanol. For the anode, 30 ml of distilled water was added to 2.0 g of commercialized ZnO, then stirred to mix well for 10 min, and the mixture was evenly dispersed on the carbon plate. After that, the prepared ZnO/C was put in the oven for 4 h at 60 °C, followed by heat treatment for 2 h at 300 °C with a 5 °C/min heating rate.

For the cathodes, the synthesis method of nano g-C_3N_4 was adopted from our previously reported work with modifications (Khor et al., 2025). A 10 ml mixture of distilled water and ethylene glycol was added to 0.3 g of synthesized nano g-C_3N_4 powder and stirred to mix well for 10 min. The nano g-C_3N_4 suspension was then evenly dispersed on the carbon plate. The loaded nano g-C_3N_4/C was put in the oven for 2 h at 60 °C, followed by heat treatment for 15 min at 200 °C with a 5 °C/min heating rate. The same procedures were used to fabricate cathodes for Cu0.5GCN9.5/C, Cu1GCN9/C, and Cu2GCN8/C.

2.5 Construction of Single and Dual Photoelectrodes Configurations PFC Systems

The single photoelectrode configurations and dual photoelectrodes configurations of the PFC system were constructed as depicted in Fig. S1 **(a)** and **(b)**, respectively. All the electrodes used in the system were prepared in a 5.00 × 3.00 × 0.30 cm. A 1 kΩ external resistor was connected to the fabricated anode and cathode in the PFC system. For all the experiments, a 400 mL beaker was filled with 300 mL of RR120 dye solution at an initial concentration of 10 mg L^{-1}, and the solution was continuously stirred using a magnetic stirrer. Air was

supplied and controlled into the dye solution at a 1 L/min flow rate by aeration stones and air pumps. A 36 W/78, 315–400 nm, 2G11 ultraviolet A (UVA) lamp from Osram Dulux was placed on the anode side of the beaker at 7 cm as a light source to irradiate the photoelectrode in the single photoelectrode PFC system while for the dual photoelectrodes PFC system, UVA lamps were placed on both side of the beaker at 7 cm as a light source to irradiate the photoelectrodes. A 2 cm distance was fixed between the anode and cathode. The PFC system was carried out at ambient temperature for a 6 h reaction time. Each experiment was replicated three times for accuracy purposes and the average values are presented as the results.

2.6 Materials Characterization

A Bruker (Model: D2 Phaser) X-ray diffraction (XRD) was applied to confirm the structural phase of the synthesized cathodic catalysts. The XRD results were recorded in a 2θ scan range at 5°- 80° with a 5°/min scanning rate. Fourier transform infrared spectra (FTIR) of the as-synthesized nano g-C_3N_4 and CuO/nano g-C_3N_4 powder were attained by a Perkin Elmer spectrophotometer (Model: Spectrum RX1 Spectrometer), by inspection of the samples in the 450–4000 cm^{-1} wavelength range. The elemental compositions and oxidation state of the synthesized samples were revealed using a Thermo Scientific X-ray photoelectron spectroscopy (XPS) (model: K-Alpha). The morphology of the samples was characterized using a field emission scanning electron microscope (FE-SEM) (Model: Nova NanoSEM 450). A thin layer of platinum was coated on the samples by a JEOL auto fine coater machine (Model: JFC-1600) to improve the production of secondary electrons and avoid charging. The bandgap energy of the samples was confirmed using a spectrophotometer (Model: Cary 100, Agilent). Micromeritics TriStar 3000 V6.06 with nitrogen adsorption–desorption analysis was used to confirm the specific surface area of all samples.

2.7 PFC Performance Analysis

The degradation efficiency of the organic pollutant was determined by using an UV–vis spectrophotometer (Model: ME-UV1200PC Mesulab, China) at $\lambda_{max} = 536$ nm to measure the absorbance of the samples. The removal efficiency was determined by using Eq. (S1) (Supplementary Information). The dye decolourisation rate was calculated using pseudo-first-order kinetics. In this model, the apparent rate constant, k_{app} was determined from the slope of the plot of ln (C_0/C) versus time (t) based on Eq. (S2) in Supplementary Information.

A ZX21e, adjustable resistor box from China, was used to perform the polarization test by varying the R_{ext} from 10 Ω to 1 M Ω, and the voltage output was observed using a CD800a, Sanwa multimeter from Japan. The current density, J_{sc} and power density, P, were determined based on Eq. (S3) and Eq. (S4), respectively (Supplementary Information).

The recyclability and transient photocurrent of the Cu0.5GCN9.5 were investigated through five consecutive cycles of experiments. After each 6-h cycle of the PFC experiment, the electrode was allowed to dry in the oven and reused for the subsequent PFC experiments.

3 Results and Discussion

3.1 Phases and Morphological Analysis

Figure 1 illustrates the FTIR spectra of nano g-C_3N_4, and different ratios of CuO coupling with nano g-C_3N_4. A peak at 810 cm^{-1} evidenced the triazine units ($C_3H_3N_3$) of nano g-C_3N_4, and the C = N stretching of nano g-C_3N_4 was related to peaks at 1568 and 1650 cm^{-1}. Furthermore, the stretch of aromatic C-N was proved by the peaks appearing at 1231, 1319, and 1409 cm^{-1}, while the adsorbed H_2O molecules (intermolecular-hydrogen bond interactions) and terminal amine units (NH or NH_2 groups) at the aromatic ring defect sites were correlated to the relatively broad peak at 3100 cm^{-1} (Fahimirad et al., 2017). For all the synthesized CuO/nano g-C_3N_4 composites, the band that appeared at 500–700 cm^{-1} could be due to the vibrational modes of CuO (Sharma et al., 2020; Sudha et al., 2021). The peak around 1622 cm^{-1} could be due to C = C (Sudha et al., 2021). In addition, it was observed that as the wt.% of CuO increased, the peaks at 683.5 cm^{-1}, indicating the presence of CuO became more prominent. Meanwhile, the peak at 1624 cm^{-1} also intensified while

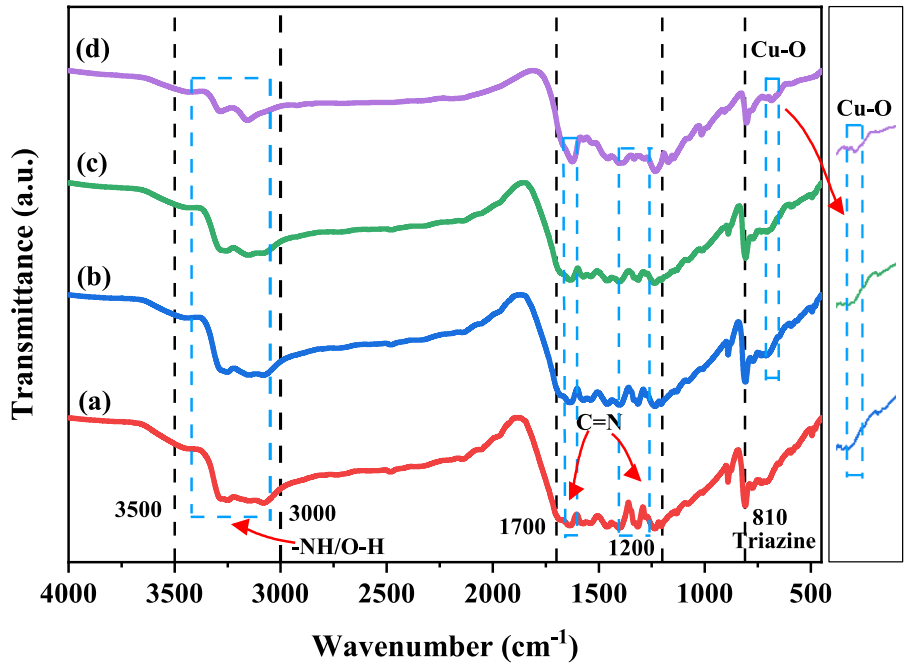

Fig. 1 FTIR pattern of **(a)** nano g-C_3N_4, **(b)** Cu0.5GCN9.5, **(c)** Cu1GCN9 and **(d)** Cu2GCN8

the peaks at 1315 cm^{-1} and the broad peak between 3000–3500 cm^{-1} decreased.

Moreover, the peak between 3000–3500 cm^{-1} declined suggests that CuO undergoes deamination during the self-polymerization of melamine at relatively high temperatures (Almeida et al., 2024; Chen et al., 2017). The 1315 cm^{-1} peak reduction may be due to the respective proportions of nano g-C_3N_4 and Cu or the formation of Cu-Nx species in the synthesized cathodic catalysts. The Cu atoms coordinated with N atoms could decrease the stretching or the skeletal vibrations of the triazine or heptazine rings. Therefore, the FTIR analysis suggests the constitution of Cu-Nx species, particularly in the Cu0.5GCN9.5, Cu1GCN9 and Cu2GCN8 cathodic catalysts, due to the Cu atoms coordinated with N atoms in the tri-s-triazine units (Zhu et al., 2019). These observations confirm the successful synthesis of nano g-C_3N_4 and the coupling of CuO in the nano g-C_3N_4 composites.

Figure 2 represents the XRD patterns of nano g-C_3N_4 and different ratios of CuO coupling with nano g-C_3N_4. Figure 2 **(a)** shows the diffraction peaks of nano g-C_3N_4 corresponding to a hexagonal crystal structure (JCPDS 87–1526, space group P62m), with two characteristic peaks observed at ~ 13.0° and ~ 27.9° (Bojdys et al., 2008; Fina et al., 2015; Nasit et al., 2025). These correspond to the in-plane motif (100) and the stacking of the graphitic carbon nitride sheet (002), respectively (Maluangnont et al., 2023). The precursor, melamine, condensed and triggered the constitution of tris-s-triazine units. These units were arranged into plates, which then interconnected through π-π* interactions, leading to the aggregation of several layers. As a result, a significant peak at around 27° was observed in the synthesized materials. This peak is associated with the (002) of the (*h k l*) diffraction plane, defined by the interplanar aromatic interaction in the aromatic heptazine rings π-π* interactions (Zandipak et al., 2024). Additionally, the diffractogram of nano g-C_3N_4 shows another, broadened peak located at approximately 13°, with (100) plane is due to the intralayer packing motif (Sunasee et al., 2019).

Figure 2 **(b–d)** presents the coupling of CuO with nano g-C_3N_4 at different ratios. In comparison to Fig. 2 **(a)**, additional diffraction peaks appeared at 36.03°, 39.23°, 49.30°, 58.27°, 61.96°, 66.44°, and 68.36° corresponding to (002), (111), (−202), (202), (−113), (−311) and (220) lattice planes, respectively. These peaks could be assigned to CuO (JCPDS 48–1548). This phenomenon indicates that CuO was successfully incorporated with nano g-C_3N_4. Moreover, it can be observed that when the CuO couples with nano g-C_3N_4, the characteristic diffraction peaks

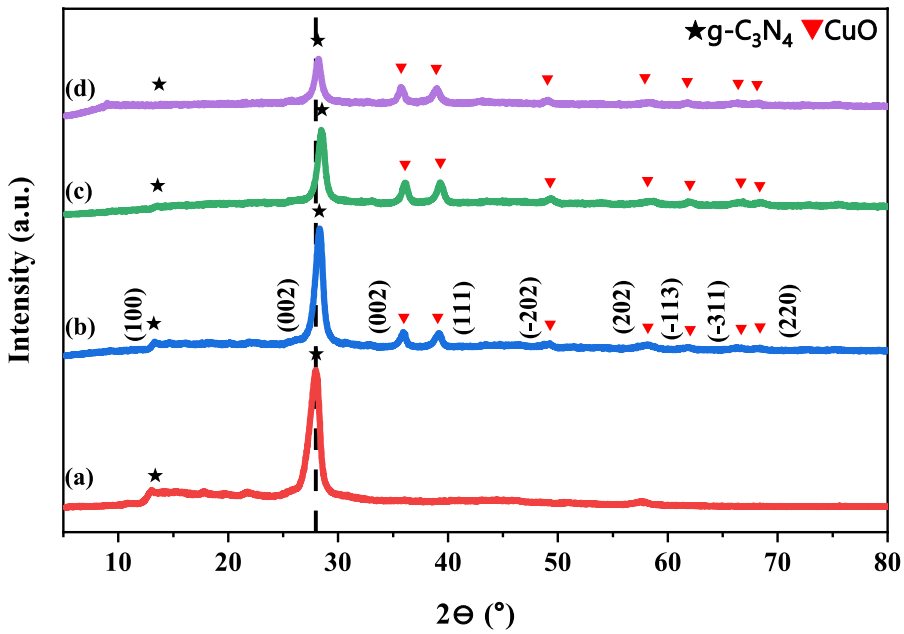

Fig. 2 XRD pattern of **(a)** nano g-C_3N_4, **(b)** Cu0.5GCN9.5, **(c)** Cu1GCN9 and **(d)** Cu2GCN8

of g-C_3N_4 are retained with shift of 0.3° to 0.6° in 2θ at 27.9°, which about 1.03–2.07% in lattice parameter c at the (002) reflections, as shown in Fig. 2. These shifts indicate that lattice distortion occurred in nano g-C_3N_4, which could be due to the incorporation of CuO altering the original arrangement of nano g-C_3N_4 and affecting the stacking between the layers (Riazati & Sheibani, 2025; Zhu et al., 2021). Furthermore, as the wt.% of CuO increased, the relative intensity of CuO increased, while the peak intensities of nano g-C_3N_4 at approximately 13° and 27.9° gradually decreased and eventually diminished in the Cu2GCN8 sample for the peak at 13°. This indicates a strong interaction between nano g-C_3N_4 and CuO and lattice distortion of the g-C_3N_4 structure upon incorporation of CuO (Sinha et al., 2025). Taken together, the XRD results and complementary FTIR analysis confirm that nano g-C_3N_4 and CuO/nano g-C_3N_4 composites were successfully synthesized

Figure 3 shows the FE-SEM images of **(a)** nano g-C_3N_4, **(b)** Cu0.5GCN9.5, **(c)** Cu1GCN9 and **(d)** Cu2GCN8, respectively. Figure 3 **(a)** demonstrated that the nano g-C_3N_4 appeared as exfoliated, loosely arranged nanosheets approximately 2–3 μm in size, with irregular agglomerates present along the edges. This observation aligned with the XRD results, where the condensation of the melamine precursor led to the formation of tris-s-triazine units. These units polymerized into sheets that interacted through π-π* stacking, resulting in the aggregation of multiple layers. Apart from that, the rough surfaces and presence of the fluffy edges of nano g-C_3N_4 indicate a thinner and dwindled structure at the nanoscale. As CuO was introduced, Fig. 3 **(b – d)** reveals that the CuO/nano g-C_3N_4 composites exhibited a flake-like morphology, with agglomerates along the edges disappearing, and CuO nanoparticles appearing on the g-C_3N_4 matrix. This agrees with the XRD analysis, which indicates there is lattice distortion occurred during the thermal polymerization of CuO/nano g-C_3N_4 composites. In Fig. 3 **(b)**, the layered structure began to fragment. At the same time, some lamellar features remained, the nano g-C_3N_4 layers became more dispersed, and surface roughness increased, indicating that CuO disrupted the orderly stacking of nano g-C_3N_4. This relatively rough surface was favorable in increasing the active sites of CuO/nano g-C_3N_4 composites, which cooperated in enhancing ORR. As the CuO content increased in Cu1GCN9 (Fig. 3 **(c)**), the disruption intensified, leading to a more agglomerated structure with diminished layering. In Fig. 3 **(d)**, Cu2GCN8, the nano g-C_3N_4 layers were almost completely lost, replaced by heavily agglomerated clusters with significant surface roughness. The gradual loss of the layered structure with increasing CuO content likely increased active sites but reduced surface area and

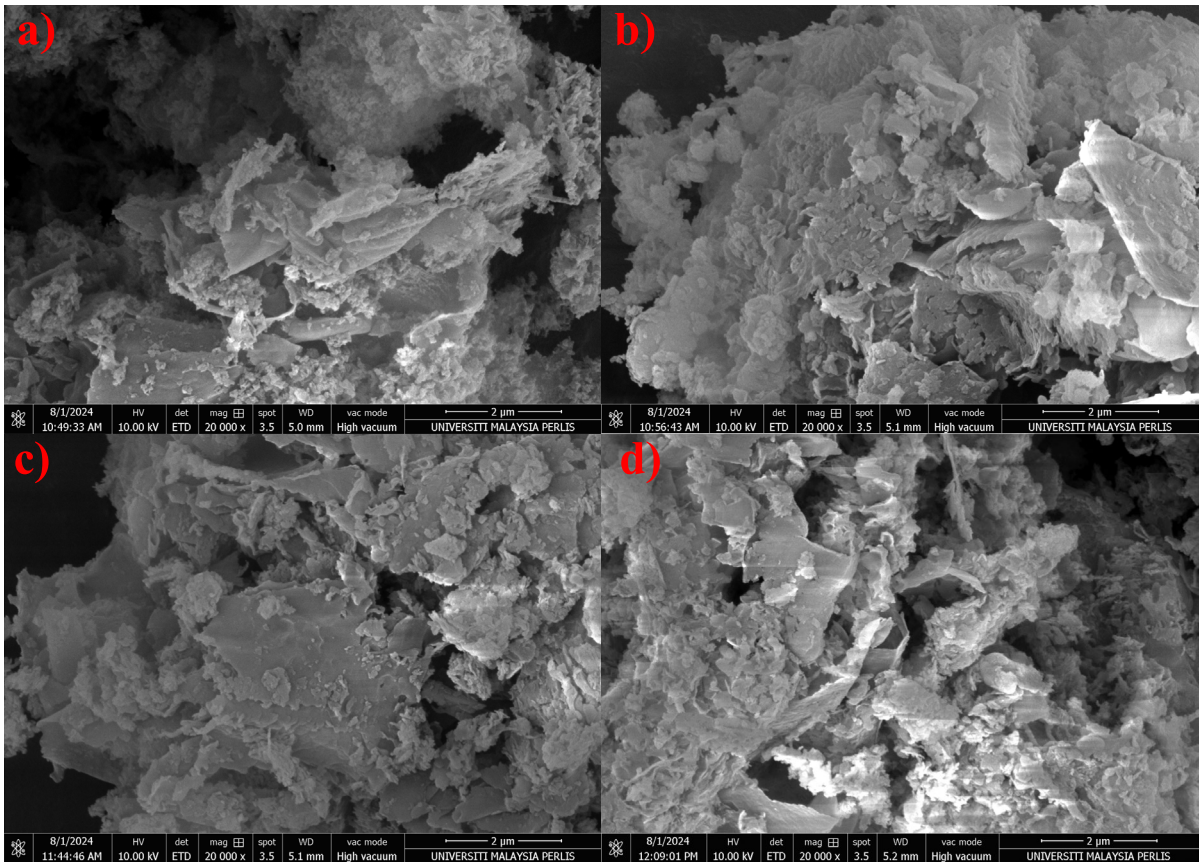

Fig. 3 FE-SEM image of **(a)** nano g-C_3N_4, **(b)** Cu0.5GCN9.5, **(c)** Cu1GCN9 and **(d)** Cu2GCN8

structural uniformity. This may improve the degradation efficiency of photocatalysis by enhancing the contact between the nanocomposite and organic pollutants (Jeevarathinam & Asharani, 2024).

3.2 Specific Surface Area Analysis

To evaluate the surface and pore properties of the prepared samples, N_2 adsorption–desorption isotherms at 77 K were carried out. The nitrogen adsorption–desorption isotherms of nano g-C_3N_4 and various CuO-to-g-C_3N_4 ratios are shown in Fig. S2. According to the IUPAC classification, all the synthesized photocathode materials exhibited type IV adsorption–desorption isotherm with a H3 type hysteresis loop, suggesting mesopore structures (diameter 2–50 nm) in the matrix with non-compact plate-like particles or slit-shaped pores that did not fully close upon desorption (Ong et al., 2021; Wang et al., 2021). Additionally, the sharp rise in adsorption at high relative pressures (P/P_0) suggested the internal of mesopores have capillary condensation, a feature consistent across all samples, likely inherent pore structure of the materials (Wang et al., 2021). Fig. S3 demonstrates the pore size distribution curves of nano g-C_3N_4, Cu0.5GCN9.5, Cu1GCN9 and Cu2GCN8 with pore sizes predominantly ranging from 20 to 50 nm, confirming mesoporous structures existed in all samples. Table 1 shows the specific surface area (S_{BET}), t-plot micropore surface area (S_{micro}) and t-plot external surface area (S_{ext}) of the synthesized samples. The BET results revealed that nano g-C_3N_4 had the highest specific surface area (71.2520 $m^2\ g^{-1}$), followed by Cu0.5GCN9.5 (48.1588 $m^2\ g^{-1}$), Cu1GCN9 (45.3213 $m^2\ g^{-1}$), and Cu2GCN8 (24.9898 $m^2\ g^{-1}$). These results were in line with the FE-SEM results, which suggest that nano g-C_3N_4 produced a thin and porous structure. Furthermore, the

Table 1 Specific surface area (S_{BET}), t-plot micropore surface area (S_{micro}) and t-plot external surface area (S_{ext}) of cathodic catalyst

Catalyst	S_{BET} ($m^2\ g^{-1}$)	t-plot S_{micro} ($m^2\ g^{-1}$)	t-plot S_{ext} ($m^2\ g^{-1}$)
Nano g-C_3N_4	71.2520	5.9958	65.2562
Cu0.5GCN9.5	48.1588	13.5507	34.6081
Cu1GCN9	45.3213	13.1138	32.2074
Cu2GCN8	24.9898	6.6795	18.3102

results demonstrate that the coupling of CuO content reduced the surface area of nano g-C_3N_4, with a marked reduction as the CuO content increased from 5 wt.% to 20 wt.%. This decline in surface area could be due to the CuO nanoparticles blocking the pores of g-C_3N_4, thus limiting the available surface area for CuO/nano g-C_3N_4 composites. Meanwhile, T-plot analyses further reveal the contributions of micropore surface area (S_{micro}) and external surface area (S_{ext}) to the total surface area of the cathodic catalysts ($S_{BET} = S_{micro} + S_{ext}$) (Zeng et al., 2020). As shown in Table 1, generally, it can be observed that when CuO is incorporated into nano g-C_3N_4, the S_{micro} of the CuO/nano g-C_3N_4 composites increased compared to pure nano g-C_3N_4. This could be due to CuO particles that created stress during thermal treatment, possibly leading to pore collapse or shrinkage in the layered nano g-C_3N_4 structure. However, as the CuO content increased, both S_{micro} and S_{ext} decreased. This trend indicated that higher CuO ratios lead to more pore blockage, reducing both microporosity and external surface area. These structural changes reflected the diminishing surface area and porosity of the composites, particularly as CuO content reached 20 wt.%, where severe agglomeration significantly reduced overall porosity. This phenomenon was compatible with the FE-SEM results, where the S_{micro} and S_{ext} were reduced by the agglomerated and attached CuO with the increment of CuO content.

3.3 Elemental Composition and Chemical State Analysis

The elemental composition and chemical states of the synthesized cathodic catalyst, Cu0.5GCN9.5, were analyzed using XPS. As shown in the chemical survey scan spectrum (Fig. 4), the presence of carbon (C 1s), nitrogen (N 1s), copper (Cu 2p), and oxygen (O 1s) was confirmed, thereby indicating the successful integration of nano g-C_3N_4 with CuO. Moreover, this finding aligns with the results of XRD and FTIR analysis, further validating the synthesis of CuO/nano g-C_3N_4.

Furthermore, high-resolution XPS spectra Fig. 4 **(b – e)** provided detailed insights into the element valence states and bonding of C, N, Cu, and O. Specifically, the deconvoluted C 1s spectrum (Fig. 4 **(b)**) revealed five peaks at 284.48 eV, 286.08 eV, 287.98 eV, 289.38 eV, and 293.58 eV. The peak at 284.48 eV was assigned to adventitious carbon (sp^2 C = C) from a thin covering of carbonaceous material on the synthesized cathodic catalyst surface (Arulkumar & Thanikaikarasan, 2024; Jeevarathinam & Asharani, 2024). Additionally, peaks at 286.08 eV and 287.98 eV were attributed to C–OH in triazine units and sp^2-hybridized C in N–C = N aromatic ring of g-C_3N_4, respectively (Vijayalakshmi et al., 2024; Zhang et al., 2023). Besides, the peaks at 289.38 eV and 293.58 eV could be attributed to metal-carbonate bonds and a satellite peak (σ* graphitic resonance) associated with carbon bonds, respectively (Chubar, 2023; Doren et al., 1994).

In the Fig. 4 **(c)**, N 1s spectrum, two significant peaks were observed at 398.58 eV and 400.48 eV, which were assigned to sp^2-hybridized N atoms (C = N–C) and bridging graphitic N atoms in the three-coordinated N-(C_3) groups, respectively (Dong et al., 2015; Vijayalakshmi et al., 2024). Furthermore, an additional peak at 404.28 eV is due to a charging effect caused by π-excitations (Wu et al., 2023). Meanwhile, the O 1s spectrum (Fig. 4 **(d)**) exhibited two main peaks at 530.38 eV and 532.08 eV, corresponding to the O 1s orbital electron state of lattice oxygen (O^{2-}) bonded to metal ions in CuO (Wang et al., 2024; Zhang et al., 2023).

The Cu 2p XPS spectrum illustrates peaks at 932.78 eV, 935.38 eV, 943.28 eV, 952.38 eV, 953.98 eV, 956.18 eV and 963.08 eV. The peaks appear at 932.78 eV and 935.38 eV correspond to the Cu $2p_{3/2}$ electron orbital state, while those at 952.38 eV and 953.98 eV are attributed to the Cu $2p_{1/2}$ electron orbital state (Shetty & Sudapalli, 2025; Yang et al., 2024). Moreover, satellite peaks around the prominent peaks at 943.28 eV and 963.08 eV confirm the presence of Cu atoms in the Cu^{2+} oxidation

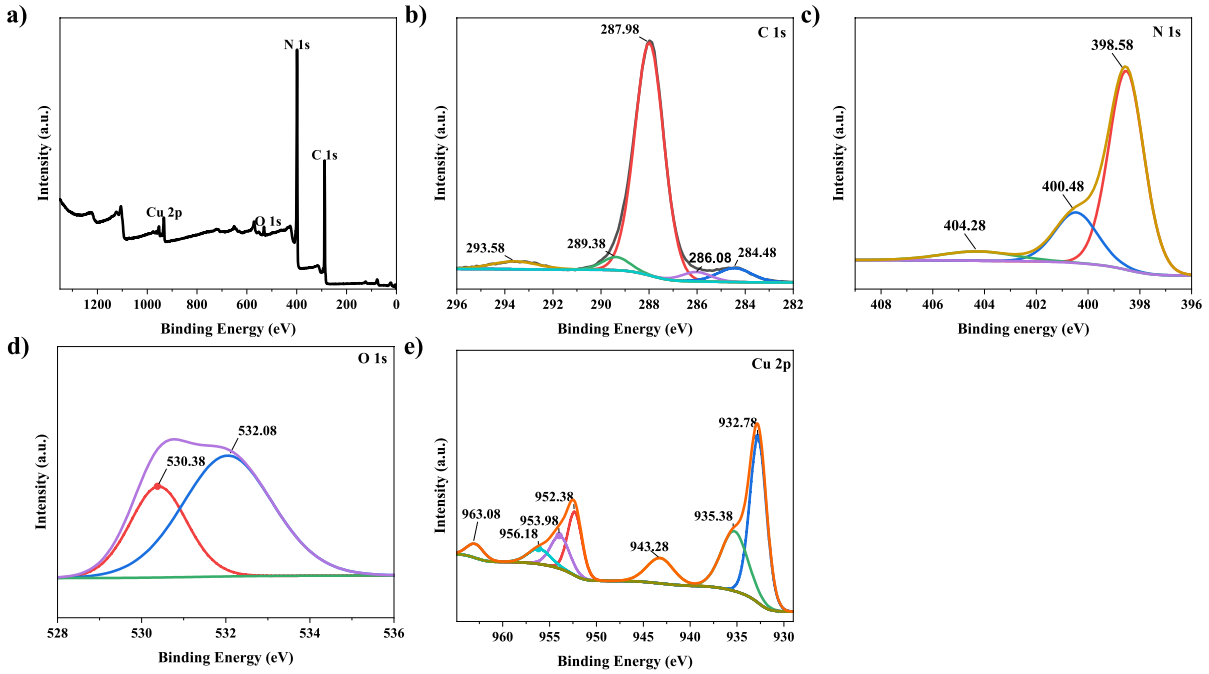

Fig. 4 XPS spectrum for **(a)** Overall scan spectrum of Cu0.5GCN9.5, **(b)** C 1s, **(c)** N 1s, **(d)** O 1s and **(e)** Cu 2p

state in the synthesized cathodic catalyst, attributable to the d^9 configuration (Majdoub et al., 2024). Therefore, it can be confirmed that the CuO/nano g-C_3N_4 composites have been successfully synthesized.

3.4 Optical Properties of Cathodic Catalysts

Optical characterization of the synthesized cathodic catalysts within the UVA and visible light ranges (360–500 nm) was performed by measuring the reflectance. Figure 5 **(a)** demonstrates the Kubelka–Munk function F(R) versus the wavelength of the synthesized cathodic catalysts. In Fig. 5 **(a)**, the composites displayed a redshift, extending their absorption into the visible light range (400–500 nm), which enhanced their photocatalytic potential under visible light. Although the composites still absorb light in the UVA region (315–400 nm), with less prominence compared to the visible range. As the CuO content increased, the absorbance rose across both UVA and visible ranges, contributing to improved photocatalytic activity, with Cu2GCN8 exhibiting the strongest absorption. This suggested that CuO enhances the photocatalytic performance of nano g-C_3N_4 under both UVA and visible light, with greater CuO content further boosting its photocatalytic activity.

From the UV–vis DRS data collected, the Kubelka–Munk method was applied to estimate the energy band gaps (E_g) of the synthesized samples. Tauc plot of nano g-C_3N_4, Cu0.5GCN9.5, Cu1GCN9 and Cu2GCN8 were constructed and shown in Fig. 5 **(b)**. The E_g of nano g-C_3N_4, Cu0.5GCN9.5, Cu1GCN9 and Cu2GCN8 were estimated to be 3.08, 2.86, 2.77 and 2.58 eV, respectively. Nano g-C_3N_4 showed a slight increase to 3.08 eV compared to a typical E_g of 2.89 eV for g-C_3N_4 and this phenomenon could be attributed to quantum confinement effects, where reduced particle size increased the E_g by restricting electron and hole movement, leading to a blue shift. (Kalisamy et al., 2020; Liu et al., 2022). When CuO was introduced, the E_g narrowed progressively, with Cu0.5GCN9.5 having a E_g of 2.86 eV < Cu1GCN9 (2.77 eV) < Cu2GCN8 (2.58 eV). The results revealed that increased CuO content led to a reduction in E_g. Consequently, CuO/nano g-C_3N_4 composites, with their lower E_g, absorbed a wider range of the light spectrum, including lower-energy visible and UVA light, which enhanced their photodegradation efficiency. Among

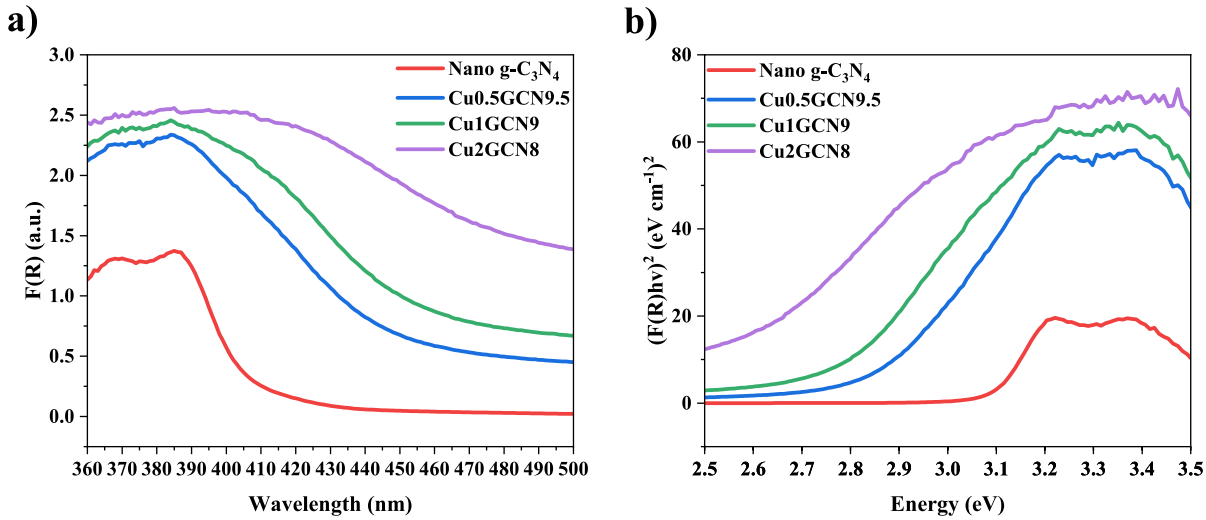

Fig. 5 **(a)** Kubelka–Munk function F(R) versus wavelength and **(b)** Tauc plot for nano g-C_3N_4, Cu0.5GCN9.5, Cu1GCN9 and Cu2GCN8

them, Cu2GCN8, with the smallest E_g, is expected to perform the best in photodegradation and the highest kinetic rate constant by utilizing more of the light spectrum. Thus, incorporating CuO into g-C_3N_4 improved the photocatalytic efficiency by narrowing the E_g and enhancing light absorption. making it more effective for photodegradation processes.

3.5 Dark-State Operation

The PFC system under dark conditions was performed to verify the role of CuO in supporting ORR within CuO/nano g-C_3N_4 composites. Since all the PFC systems utilized the same anode, flow rate and volume of organic pollutants, the degradation of RR120 was entirely dependent on the cathodic materials. In the absence of light irradiation, there was no photocatalytic reaction occurring. However, the organic pollutants can be degraded by direct oxidation via direct electron transfer (Wang et al., 2023). In this study, ZnO/C, as an anode under dark conditions, still functions as a catalyst, facilitating electrochemical oxidation rather than photogenerated electron–hole pair formation, thereby producing electrons that were moved to the cathode via the external connection (Phuong Thi Minh et al., 2019). Besides, organic pollutant adsorption onto the electrode surfaces (ZnO/C as the anode and the bare carbon plate as the cathode) contributed to its removal (K K et al., 2024).

Figure 6 shows the RR120 color removal efficiency during a 6-h reaction period under dark conditions. As shown in Fig. 6, nano g-C_3N_4/C, as a cathode in the PFC system, showed the lowest color removal efficiency (14.13%) and generated the lowest maximum power output (P_{max}) of 0.00001 mW/m^2. The generation of electricity provided evidence that ORR occurred, as electricity needed the transportation of electrons to the cathode from the photoanode for ORR to take place. This finding indicated that, besides adsorption, electrocatalytic activity also contributed to color removal in the PFC system. Furthermore, when CuO was introduced in nano g-C_3N_4, the performance of PFC systems of CuO/nano g-C_3N_4 cathodic catalysts as the cathode showed a significant enhancement as compared to nano g-C_3N_4. It can be observed that a higher CuO wt.% led to notable improvements in both color removal efficiency and electricity generation. The PFC system of Cu0.5GCN9.5, with the lowest CuO wt.%, exhibited nearly double the color removal efficiency (27.67%) compared to nano g-C_3N_4 (14.13%). However, no significant improvement in electricity generation was observed as almost the same P_{max} (0.0001 mW/m^2) for both PFC systems. In contrast, the PFC system of Cu2GCN8 with the highest CuO wt.%, achieved a color removal efficiency of 50.14% and a power output of 0.0013 mW/m^2. These findings suggest that under dark conditions, increasing the CuO

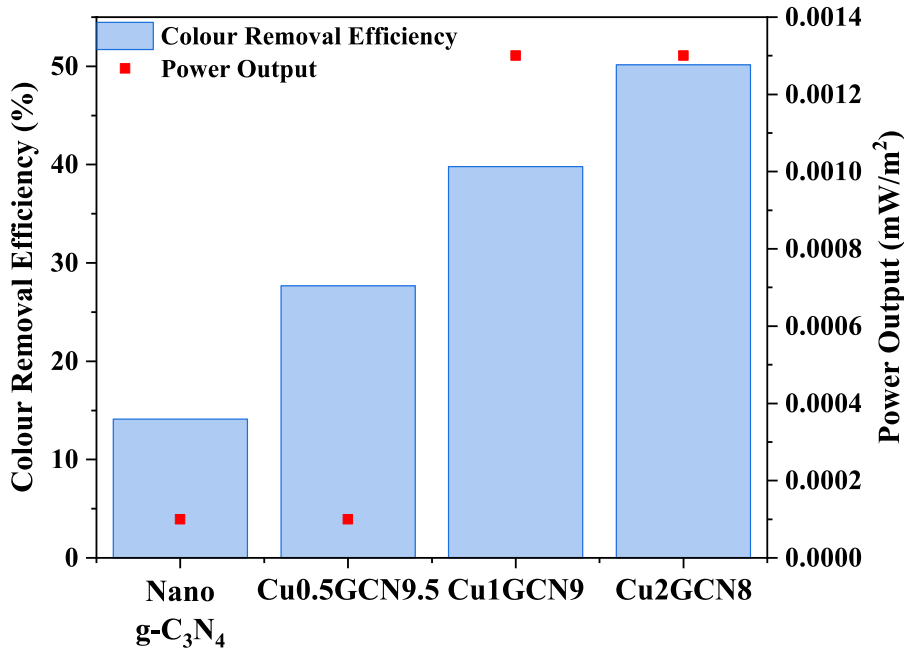

Fig. 6 Performance of PFC with different cathodes under dark conditions

wt.% in CuO/nano g-C_3N_4 composites enhances the PFC system's performance in terms of color removal efficiency and electricity generation facilitated by the ORR activity.

3.6 Photolysis of RR120 under UVA Light Irradiation

To investigate the effect of UVA light on the 10 mg L^{-1} of RR120 degradation, the photolysis of RR120 was conducted under both single light and dual light sources. Photolysis is an experiment in which light is directly irradiation to synthetic dye or organic wastewater, without the addition of photocatalysts, ensuring that the degradation of the synthetic dye or organic pollutant is solely dependent on the light exposure. To confirm the effect of UVA light on the RR120, the photolysis was conducted under identical conditions as the PFC systems but without electrodes for a 6-h reaction time. **Fig. S4** shows the UV–Vis spectra of RR120 photolysis under (a) single UVA light irradiation and (b) dual UVA light irradiation. As shown in **Fig. S4 (a)** and **(b)**, no significant degradation of RR120 was observed at the azo bond peak, -N = N- (~ 536 nm), or at the peak corresponding to benzene and naphthalene rings (~ 300 nm) under either condition. The results disclosed that the UVA light alone does not contribute to the degradation of RR120 under a 6-h reaction time. Therefore, it can be concluded that the degradation of RR120 in PFC systems, whether under single or dual photoelectrode configurations, was entirely dependent on the PFC system, as all the other parameters were identical for all experiments.

3.7 Effect of Different Cathode Materials on Degradation under Single and Dual Photoelectrodes Configurations

The impact of nano g-C_3N_4 and CuO/nano g-C_3N_4 composites as cathodes on the degradation of organic pollutants in the PFC system under single and dual photoelectrode configurations was investigated. Figure 7 **(a)** and **(b)** demonstrate the 10 mg L^{-1} RR120 color removal efficiency over irradiation time with different cathodes in PFC under single and dual photoelectrodes configurations, respectively. Under the single photoelectrode configurations, nano g-C_3N_4 achieved a color removal efficiency of 85.19%. This could be due to under single photoelectrode configurations, the nano g-C_3N_4 cathode has not been activated and just ORR activity happened, producing $\bullet O_2^-$ (Eq. 4) to facilitate the degradation. In contrast, under dual photoelectrode configurations, its efficiency increased to 96.83%, which is 1.13-fold higher than the single photoelectrode configurations,

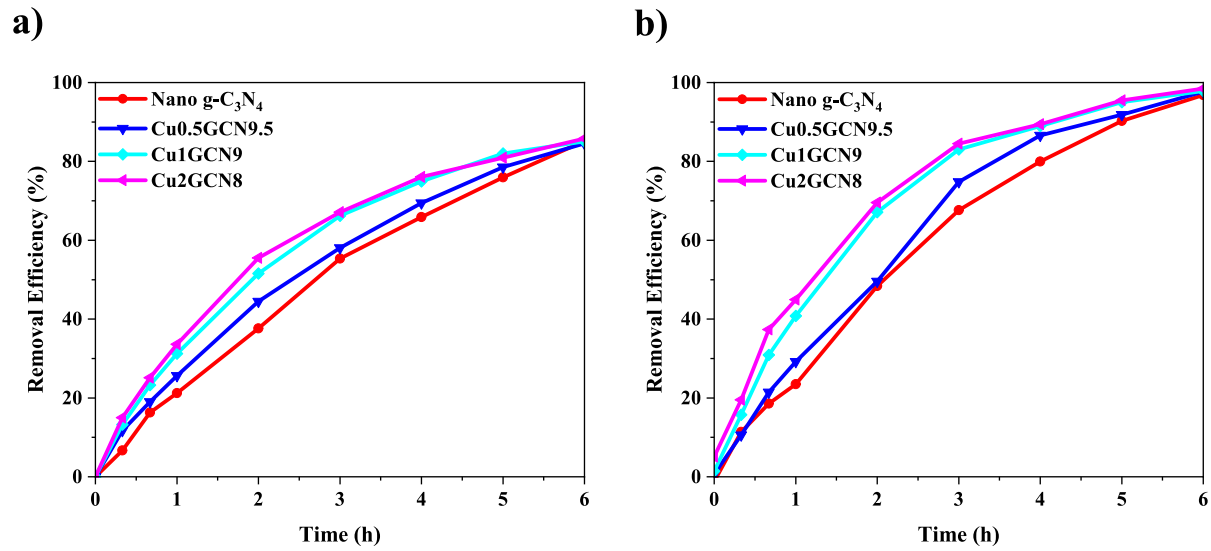

Fig. 7 10 mg L^{-1} RR120 color removal efficiency over irradiation time with different cathodes in PFC system under **(a)** single photoelectrode configurations and **(b)** dual photoelectrode configurations

demonstrating the advantage of the dual photoelectrodes PFC system. The prominent photocatalytic activity of nano g-C_3N_4 PFC system under dual photoelectrodes configurations was attributed to the stimulation of light toward photocatalysts, which led to the generation of electron–hole pairs and enhanced the degradation of the RR120 (Eq. 1, 2 & 3). This improved the degradation of RR120 by producing reactive oxygen species (ROS), •OH and $\cdot O_2^-$ (Eq. (4) & Eq. (5)), which further enhanced the degradation efficiency. Besides that, this enhanced the migration of electrons from the conduction band (CB) of the photoanode to the valence band (VB) of the photocathode due to there being more electron–hole pairs generated, thus facilitating electron transfer, boosting the ORR at the cathode, and improving the decolorization efficiency of the PFC systems.

$$\text{Photocathode} + \text{hv (light)} \rightarrow \text{Photocathode}\left(e_{CB}^- + h_{VB}^+\right) \quad (1)$$

$$\text{Photocathode}\left(h_{VB}^+\right) + H_2O \rightarrow \text{H}^+ + \cdot\text{OH} \quad (2)$$

$$\cdot OH + RR120 \rightarrow degraded\ products + e^- \quad (3)$$

$$e^- + \text{O}_2 \rightarrow \cdot O_2^- \quad (4)$$

$$\bullet O_2^- + \text{RR120} \rightarrow \text{degraded products} \quad (5)$$

Nonetheless, when nano g-C_3N_4 coupled with CuO as the cathode in the PFC systems under single photoelectrodes configurations, the Cu2GCN8 system achieved the highest decolorization efficiency (85.82%) after 6 h, compared to nano g-C_3N_4 (85.19%), Cu1GCN9 (85.04%), and Cu0.5GCN9.5 (84.54%) systems. The efficiency of a photocatalyst in generating electron–hole pairs is a key factor in the photodegradation reaction (Mubeen et al., 2023). When the PFC systems were conducted under the dual photoelectrode configurations, the decolorization efficiency significantly improved compared to single photoelectrodes (Fig. 8). Specifically, the Cu2GCN8 exhibited the highest efficiency at 98.46%, followed by the Cu1GCN9 (97.84%), Cu0.5GCN9.5 (97.69%), and nano g-C_3N_4 (96.83%). This could be due to light activation of CuO enhancing the photogenerated charge in nano g-C_3N_4, which makes CuO/nano g-C_3N_4 have more active sites or holes (h^+) for RR120 oxidation. In addition, it was worth noting that during dual photoelectrode configurations, a higher CuO-to-g-C_3N_4 ratio consistently improved decolorization efficiency. This enhancement could be attributed to increased CuO content in CuO/nano g-C_3N_4 composites, thus improving the optical properties of CuO/nano composites and increasing the

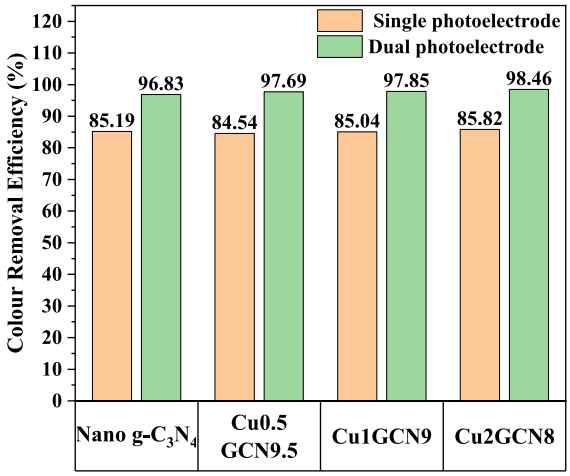

Fig. 8 Comparison of RR120 color removal efficiency at 10 mg L^{-1} with different photocathodes in PFC under single and dual photoelectrode configurations

number of active sites, which were discussed before in Sect. 3.2. UVA light irradiation further facilitated photocatalytic reactions at the photocathode, promoting electron–hole pair separation and continuous degradation, thereby enhancing color removal efficiency. These findings indicate that dual photoelectrode configurations significantly improve the degradation performance of the PFC system compared to single photoelectrode setups. Furthermore, optimizing the optical properties of CuO/nano g-C_3N_4 composites could further enhance organic pollutant degradation.

The impact of nano g-C_3N_4 and CuO/nano g-C_3N_4 composites as cathodes on the degradation of organic pollutants in the PFC system under single and dual photoelectrode configurations was investigated. The behaviour of degradation of organic pollutant was examined by plotting the relationship between RR120 concentration (C/C_0) and irradiation time, as shown in Fig. 9 **(a)** and **(b)**. In Fig. 9 **(a)** and **(b)**, as the reaction proceeds, the cathodic catalysts in the dual photoelectrode configuration manifested a sharper decrease in C/C_0 compared to the single photoelectrode configuration, indicating a higher removal rate of RR120. This revealed that the cathodic catalysts with the dual photoelectrode configuration PFC system possessed higher photocatalytic activity, which could be observed at t = 3. All the cathodic catalysts in the dual photoelectrode configuration possessed superior photocatalytic activity (nano g-C_3N_4 = 0.3238, Cu0.5GCN9.5 = 0.2517, Cu1GCN9 = 0.1697, and Cu2GCN8 = 0.1551) compared with the respective cathodic catalysts in the single photoelectrode configuration (nano g-C_3N_4 = 0.4465, Cu0.5GCN9.5 = 0.41924, Cu1GCN9 = 0.3381, and Cu2GCN8 = 0.1551). This enhancement could be attributed to the activation of the photocathode to

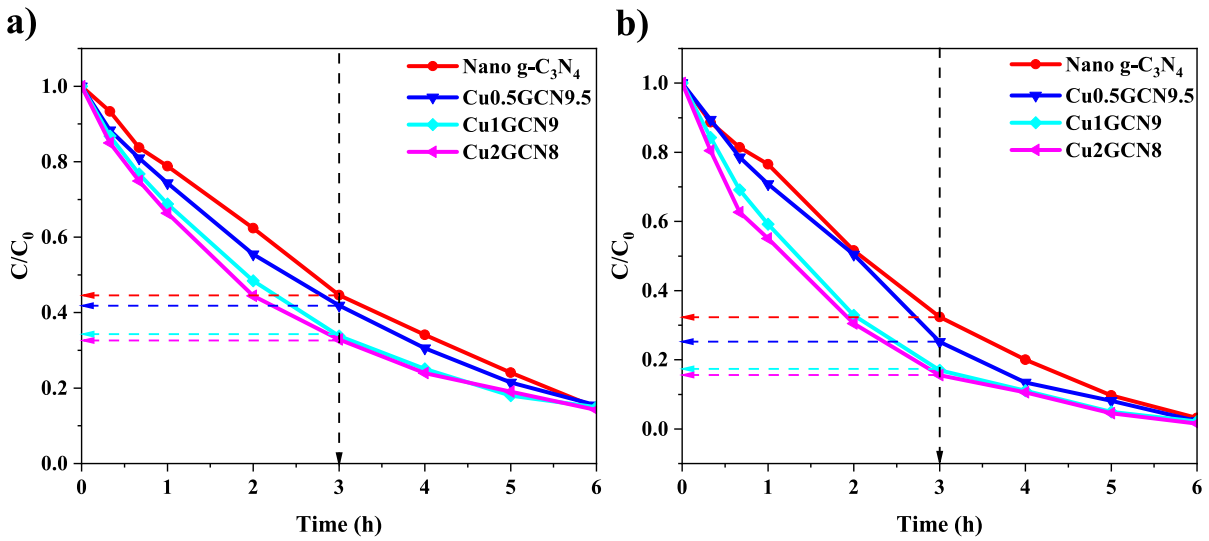

Fig. 9 Plot of C/C_0 over irradiation time with different cathodes in PFC system at 10 mg L^{-1} under **(a)** single photoelectrode configurations and **(b)** dual photoelectrode configurations

create electron–hole pairs, which enhanced the oxidation of RR120 under UVA light irradiation in dual photoelectrode configurations. Furthermore, it could be observed that for both single and dual photoelectrode configurations, the photocatalytic activity improved as the CuO was incorporated into nano g-C_3N_4, and the photocatalytic activity kept accelerating as the wt.% of CuO increased up to 10 wt.% of CuO. Further increasing the CuO content to 20 wt.% in the composite could hardly improve the photocatalytic activity as the removal rate of RR120 was only found to increase slightly. This indicated that incorporating CuO into the g-C_3N_4 could enhance the photocatalytic activity up to 20 wt.% of CuO in g-C_3N_4.

Fig. 10 **(a)** and **(b)** represent the kinetic photocatalytic degradation for 10 mg L^{-1} of RR120 over irradiation time with different cathodes in the PFC system under single and dual photoelectrodes configurations, respectively. Table 2 summarises the kinetic rate based on the Langmuir–Hinshelwood kinetic model for 10 mg L^{-1} of RR120 over irradiation time with different cathodes in PFC under single and dual photoelectrode configurations. As shown in Table 2, all the kinetics models accurately suited the experimental data with a good correlation factor ($R^2 \approx 1$), validating a positive agreement for the suited models with experimental results (Ong et al., 2019). In the single photoelectrode configuration, Cu2GCN8 showed the highest apparent rate constant, k_{app}, compared to other photocathode materials in this study, in which Cu2GCN8 (0.3443 h^{-1}) > Cu1GCN9 (0.3401 h^{-1}) > Cu0.5GCN9.5 (0.3080 h^{-1}) > nano g-C_3N_4 (0.2910 h^{-1}). While the k_{app} of different photocathode materials for PFC under dual photoelectrodes

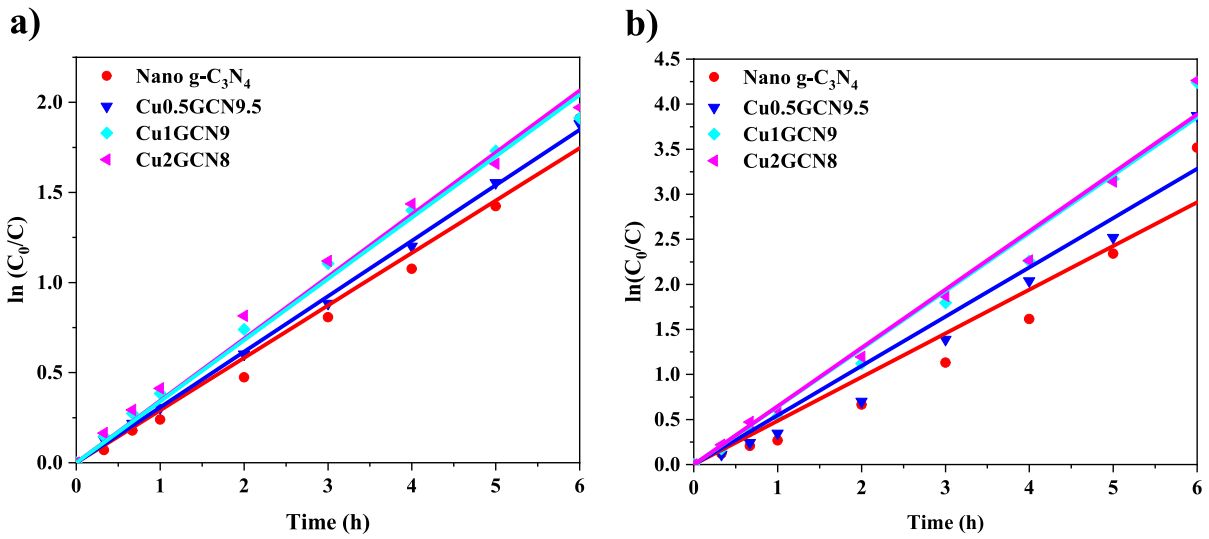

Fig. 10 Kinetic photocatalytic degradation for 10 mg L^{-1} of RR120 over irradiation time with different cathodes in PFC system under **(a)** single photoelectrode configurations and **(b)** dual photoelectrode configurations

Table 2 Apparent rate constant, k_{app} (h^{-1}) of Pseudo-first order for different photocathodes

Cathodes	Single-photoelectrode		Dual-photoelectrodes	
	Apparent rate constant, k_{app} (h^{-1})	Goodness-of-fit, R^2	Apparent rate constant, k_{app} (h^{-1})	Goodness-of-fit, R^2
Nano g-C_3N_4	0.2910	0.9929	0.4852	0.9667
Cu0.5GCN9.5	0.3080	0.9994	0.5470	0.9752
Cu1GCN9	0.3401	0.9967	0.6241	0.9909
Cu2GCN8	0.3443	0.9953	0.6477	0.9919

configuration increased significantly, following the order: nano g-C_3N_4 (0.4852 h^{-1}) < Cu0.5GCN9.5 (0.5470 h^{-1}) < Cu1GCN9 (0.6241 h^{-1}) < Cu2GCN8 (0.6477 h^{-1}). When the PFC systems were switched from single photoelectrodes configuration to dual photoelectrodes configurations, the k_{app} of the PFC systems increased and varied from about 40% to 47%, the trends consistent with the decolorization efficiency of RR120. This improvement indicates that dual photoelectrode configurations boosted the performance of the PFC system in terms of color removal efficiency by activating the photocatalyst with light, facilitating electrons transfer to O_2 since photocathode have the properties to perform oxidation of organic pollutant and released electrons, which provided more electrons to enhance cathodic ORR activity and production of $\bullet O_2^-$, thus giving a notable increment in the k_{app} and decolorization of RR120

Additionally, it could be noticed that CuO/nano g-C_3N_4 composites as cathode possessed a higher k_{app} than pristine nano g-C_3N_4 in both configurations of PFC systems. This improvement could be due to the synergistic effects of CuO and nano g-C_3N_4, which promoted the ORR and enhanced decolorization efficiency. Furthermore, it is worth noting that the k_{app} increased with higher CuO content. In this study, increasing the CuO loading led to a reduction in the band gap of the cathodic materials (Sect. 3.4). The reduction of the band gap resulted in large wavelength absorption, hence improving the photocatalytic degradation and enhancing the k_{app} (Khatun et al., 2023). Among these, the PFC system of Cu2GCN8 with the highest CuO content exhibited the highest $k_{app,}$ demonstrating the fastest color removal rate under both single and dual photoelectrodes configurations. This could be attributed to its relatively minor band gap, which enhanced light absorption and charge utilization in the reaction. Since all PFC system setups in this study were identical except for the cathodic catalysts, it can be inferred that the increasing CuO content in nano g-C_3N_4 enhanced the photocatalytic activity, thereby improving the degradation of RR120. Consistent with the results of the degradation efficiency in both configurations, it can be observed that the PFC systems with dual photoelectrodes configurations and CuO/nano g-C_3N_4 composites promoted higher degradation efficiency and kinetic rate than single photoelectrode configurations.

To verify the degradation of the organic pollutant during the PFC operation, UV–Vis spectra measurements were conducted. Figure 11 illustrates the time-dependent UV–Vis absorption spectra of the RR120 under **(a)** single photoelectrode and **(b)** dual photoelectrode configurations for the Cu0.5GCN9.5. As seen in both configurations, the characteristic absorption peaks at approximately 300 nm and 536 nm, corresponding to the benzene and naphthalene rings and –N = N– azo group of RR120, respectively, gradually decrease with increasing irradiation time, indicating the progressive breakdown of the dye molecules. The destruction of these peaks after 6 h of PFC operation confirms the degradation of RR120.

3.8 Effect of Different Cathode Materials on Electricity Generation Under Single and Dual Photoelectrodes Configurations

Fig. 12 **(a)** and **(b)** display the polarization curve and power density curve of the PFC system with different cathodes under single and dual photoelectrode configurations, respectively. Since all the PFC system setups were consistent in this study, variations in performance could be attributed completely to the differences in the cathodes, either in single or dual photoelectrodes configurations. Significant differences in electricity generation are observed for the PFC system with different cathode materials. In a fuel cell, the maximum power output can be obtained when the load resistance (R_L) is equivalent to its R_{int} (Ong et al., 2019). A PFC system with lower internal resistance (R_{int}) generally enhances the maximum power density (P_{max}) of the system (Guadarrama-Pérez et al., 2024). As the R_{int} of the PFC system decreases, it is expected that the charge separation and electron transfer efficiency from the anode to the cathode will improve. This subsequently enhances the ORR activity by accepting electrons at the cathode and thus generating higher electricity.

Table 3 summarizes the electricity generation performance of PFC systems with different cathodes (CuO/g-C_3N_4 and Pt-based systems) under single and dual photoelectrode configurations. Under single photoelectrode configuration, the pristine nano g-C_3N_4 showed a relatively low R_{int} (5448.72 Ω) with P_{max} = 0.43 mW/m^2, while pristine nano g-C_3N_4 under dual photoelectrodes showed an increment in R_{int} (6992.17 Ω) and a doubled P_{max} = 1.02 mW/m^2. This increase in R_{int} may

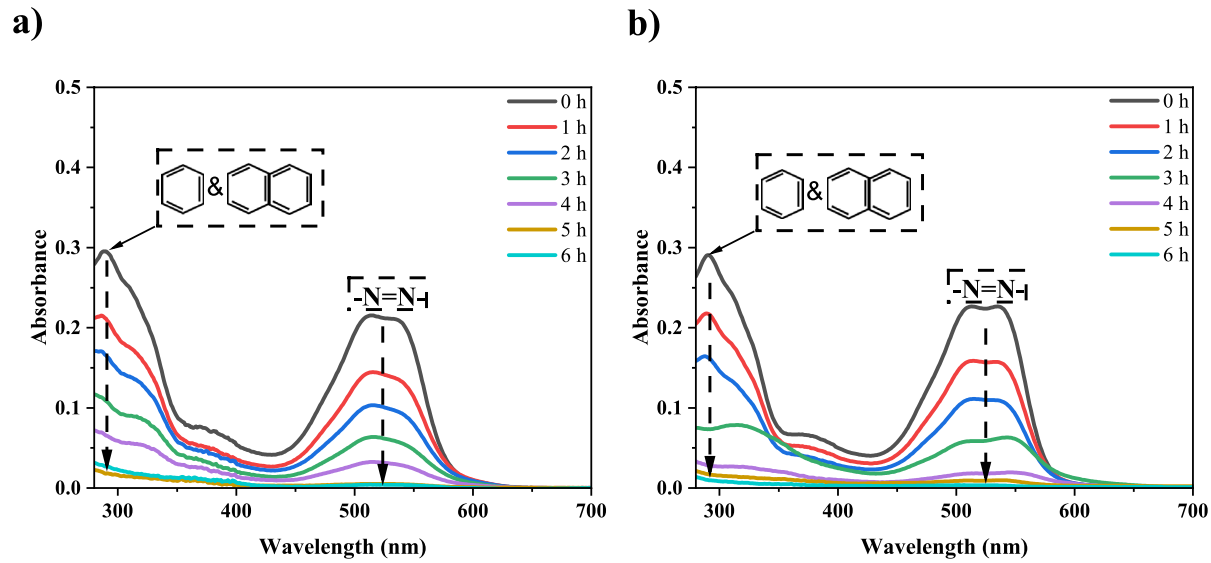

Fig. 11 Time-dependent UV–Vis absorption spectra of the RR120 under **(a)** single photoelectrode and **(b)** dual photoelectrode configurations for Cu0.5GCN9.5

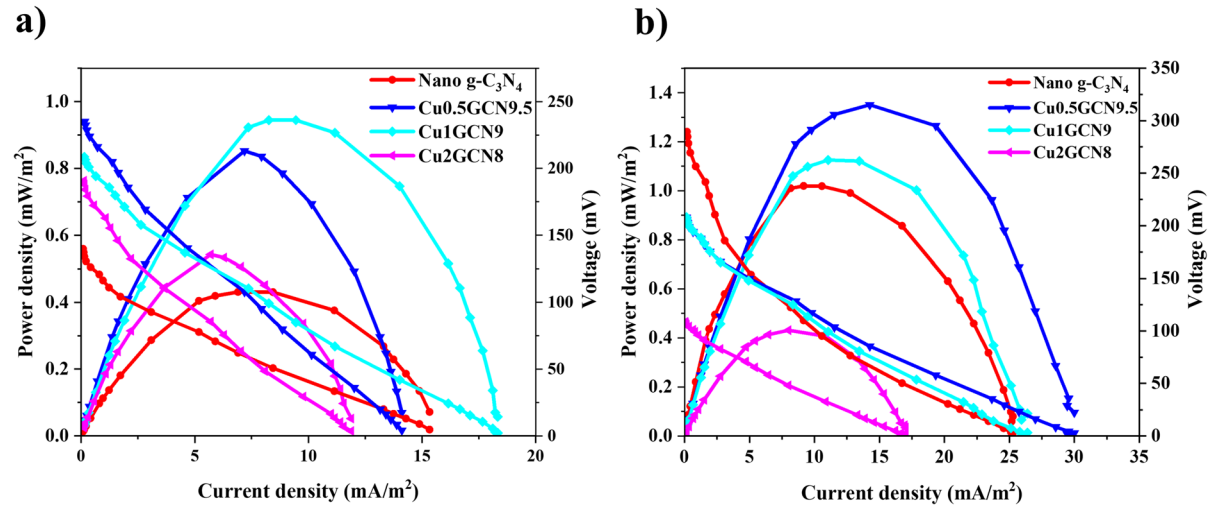

Fig. 12 Polarization curve and power density curves of PFC system with different cathodes under **(a)** single photoelectrode configurations and **(b)** dual photoelectrode configurations

be contributed to under dual photoelectrodes configurations, the nano g-C_3N_4 under light irradiation would have the properties of the anode and cathode, resulting in the degradation of organic pollutants (oxidation process) and the release of electrons and H^+ ions into the electrolyte, which increased ionic concentration. The increased ionic concentration might affect charge transport dynamics, but more significantly, the excess electrons generated in the system accumulated at the cathode due to the inherently sluggish ORR activity of pristine nano g-C_3N_4. This charge buildup hinders efficient electron transfer, thereby increasing R_{int}. Despite this, the dual-photoelectrodes PFC system benefits from an enhanced photovoltage, which improved charge separation and facilitated higher power output, ultimately leading to a significant increase in P_{max}.

As nano g-C_3N_4 was incorporated with increasing CuO content, the R_{int} of cathodic catalysts increased under single photoelectrode conditions (Cu0.5GCN9.5 = 10,651.30 Ω; Cu1GCN9 = 7247.29

Table 3 Electricity generation performance of PFC systems with different cathodes (CuO/nano g-C_3N_4 and Pt-based systems) under single and dual photoelectrode configurations

Cathode	V_{oc} (mV)	J_{sc} (mA/m^2)	P_{max} (mW/m^2)	R_{int} (Ω)	η (%)	Photo-electrode	References
Nano g-C_3N_4	139.77	15.56	0.43	5448.72	1.80	Single	Current study
	289.37	25.19	1.02	6992.17	4.25	Dual	Current study
Cu0.5GCN9.5	235.00	14.07	0.85	10651.30	3.55	Single	Current study
	207.87	30.00	1.35	4420.12	5.63	Dual	Current study
Cu1GCN9	208.57	18.15	0.94	7247.29	3.94	Single	Current study
	208.20	29.93	1.13	5094.51	4.69	Dual	Current study
Cu2GCN8	190.70	11.85	0.54	10108.96	2.26	Single	Current study
	108.63	17.04	0.43	4145.62	1.79	Dual	Current study
Pt/C	Not specified	41.00	2.80	Not specified	Not specified	Single	(Lee et al., 2018)
Pt	500.00	58.60	89.00	Not specified	Not specified	Single	(Deng et al., 2018)
Pt/C	355.30	56.00	5.28	Not specified	Not specified	Single	(Ong et al., 2019)
Pt/C	455.00	788.00	91.78	Not specified	7.08	Single	(Ong et al., 2020)
Pt	414.00	Not specified	27.07	Not specified	Not specified	Single	(Yong et al., 2022)
Pt/C	328.80	237.04	17.14	Not specified	Not specified	Single	(OrYang et al., 2025)

Ω; Cu2GCN8 = 10,108.96 Ω) but was accompanied by an increased in P_{max} for Cu0.5GCN9.5 (0.85 mW/m^2), Cu1GCN9 (0.94 mW/m^2) and Cu2GCN8 (0.54 mW/m^2), compared to pure nano g-C_3N_4 (5448.72 Ω; P_{max} = 0.43 mW/m^2). The increase in R_{int} when CuO is incorporated into nano g-C_3N_4 could be attributed to CuO remaining inactive as a semiconductor in the absence of UVA light irradiation. Consequently, insufficient photoactivation of CuO increases internal resistance by introducing additional charge transfer barriers, leading to higher R_{int} in CuO/nano g-C_3N_4 composites. Despite the higher internal resistance of CuO/nano g-C_3N_4 composites, the presence of CuO in Cu0.5GCN9.5, Cu1GCN9 and Cu2GCN8 still improved photocatalytic activity, resulting in higher P_{max} compared to pristine nano g-C_3N_4. This tendency could be attributed to the potential of CuO/nano g-C_3N_4 composites as electron acceptors due to CuO being a p-type semiconductor, which has more electronegativity.

Under dual photoelectrodes configurations, the R_{int} of cathodic catalysts (Cu0.5GCN9.5 = 4420.12 Ω; Cu1GCN9 = 5094.51 Ω) was significantly reduced, resulting in enhanced electricity generation (Cu0.5GCN9.5: P_{max} = 1.35 mW/m^2; Cu1GCN9: P_{max} = 1.13 mW/m^2) compared to their single photoelectrode counterparts. This could be due to the photoactivation of both CuO and nano g-C_3N_4 under UVA light irradiation, which induced a synergistic effect between the two materials. This resulted in an internal electric field formed at the interface of CuO and nano g-C_3N_4, improved interfacial charge transfer at the CuO-g-C_3N_4 junctions, and enhanced electron mobility. This field reduced the electron–hole pairs recombination, thus facilitating the ORR and improving power output when the CuO/nano g-C_3N_4 composites were under light irradiation (Qin et al., 2025). Interestingly, despite Cu2GCN8 exhibiting the lowest R_{int} (4145.60 Ω), its power output (J_{sc} = 17.04 mA/m^2 and P_{max} = 0.43 mW/m^2) was lower than Cu0.5GCN9.5, Cu1GCN9 and even the pristine nano g-C_3N_4. This abnormal phenomenon can be explained by CuO trapping electrons on its surface or at interfaces (Bandaranayake et al., 2024; Van Cakenberghe et al., 1981). The results revealed that it acted as an efficient photocathode when it was in lower or optimum ratios of CuO and g-C_3N_4. However, when the ratio of CuO is too high in CuO/nano g-C_3N_4, the CuO traps excessive electrons, leading to increased charge recombination. As a result, instead of facilitating efficient electron movement from the anode to the CuO/nano g-C_3N_4 cathode, the reaction is hindered, limiting the ORR activity and reduced power output. Overall, the results suggest that while reducing R_{int} is essential for improving the electricity generation in PFC, other factors, such as ratios of CuO to nano

g-C_3N_4, must also be optimized. Among the cathodic catalysts, Cu0.5GCN9.5 under dual photoelectrodes configurations PFC system exhibited the best overall balance between low R_{int} and the highest electricity generation.

In this study, V_{oc} is an important parameter that evaluates the photoelectrochemical activity of the cathode materials. It is the maximum voltage produced by the PFC under zero drawn current and is affected by the charge separation efficiency, recombination losses of the system (Blakesley & Neher, 2011). A higher V_{oc} typically represents higher photogenerated charge carrier separation and lower recombination. Under single photoelectrode configurations, Cu0.5GCN9.5 recorded the highest V_{oc} (235.00 mV), which suggests that CuO incorporation is attributable to enhanced charge separation by producing a heterojunction with nano g-C_3N_4. On the contrary, nano g-C_3N_4 exhibited a lower V_{oc} (139.70 mV), likely due to its limited capability in charge separation. But in the dual-photoelectrode setup, nano g-C_3N_4 reflected significantly higher V_{oc} (289.37 mV), which was the highest among all samples. This improvement may be attributed to symmetric illumination of both electrodes, which activated nano g-C_3N_4 to generate electron–hole pairs. The photogenerated holes and electrons facilitated RR120 degradation and ORR activity at the cathode, reducing recombination losses and enhancing electron flow from anode to cathode, thereby optimizing the photovoltage output. Despite the high V_{oc}, nano g-C_3N_4 showed a relatively lower P_{max} (1.02 mW/m^2) compared with Cu0.5GCN9.5 (1.35 mW/m^2), reflecting its inherent limitations in photocurrent generation and charge transport.

Additionally, CuO incorporation with nano g-C_3N_4 enhances the power output at the cathode on optimum ratios, as evidenced by the higher J_{sc} values observed for CuO-modified catalysts compared to nano g-C_3N_4 alone (Table 3). It was reported that materials with efficient light absorption, charge separation, transport, and collection are required to produce high J_{sc} (Khampuanbut et al., 2024; Zhao et al., 2022). Under dual light conditions, the J_{sc} of Cu0.5GCN9.5 and Cu1GCN9, which achieves relatively higher J_{sc} 30.00 mA/m^2 and 29.93 mA/m^2, respectively compared to pure nano g-C_3N_4 (25.19 mA/m^2), indicating CuO enhanced electricity generation of the systems by making the composites become more effectively in light absorption, charge separation and charge collection at the cathode (Lie et al., 2018). Thus, the performance of electricity generation of the PFC systems decreased, followed by the order of Cu0.5GCN9.5 > Cu1GCN9 > nano g-C_3N_4 > Cu2GCN8. The Cu0.5GCN9.5 has the highest performance could be due to improved light absorption and enhanced charge separation, resulting in a higher ORR activity, as evidenced by significant differences in cathode potential, with all systems being identical.

Since the energy conversion efficiency in PFC mainly relies on the ORR activity, the greater the energy conversion efficiency (η) of the PFC system, the higher the ORR activity at the cathode. Among all the photocathodes, Cu0.5GCN9.5 demonstrated the highest η, particularly under the dual-photoelectrode configuration, achieving 5.63% efficiency with a well-balanced V_{oc} (207.87 mV) and J_{sc} (30.00 mA/m^2). This could be attributed to the optimal incorporation of CuO into nano g-C_3N_4, which enhanced light absorption, promoted efficient charge separation through heterojunction formation, and improved ORR activity as well as maintaining a relatively low R_{int}. These combined properties made Cu0.5GCN9.5 the most effective photocathode for electricity generation in the dual photoelectrode configuration in the PFC system.

To further evaluate the performance of the prepared CuO/nano g-C_3N_4 composites, the obtained power output values were compared with those reported in a previous study in Table 3. The reference study employed Pt-based cathode materials but used a comparable PFC configuration, allowing for a meaningful comparison. As shown in Table 3, the power output values of the synthesized composites were lower than those of Pt-based systems, which could be due to the superior intrinsic ORR activity of Pt (Madima & Raphulu, 2025; Ouyang et al., 2022; Qin et al., 2022). Although Pt-based PFC systems exhibit higher V_{oc}, J_{sc}, and η values compared to CuO/nano g-C_3N_4 composites, their high cost and scarcity limit their large-scale application. In this study, the results demonstrated that CuO/nano g-C_3N_4 composites could operate as cost-effective, sustainable cathode materials and fulfill the primary objective of this work, which is to explore an alternative cathode material to

enhance pollutant degradation and ORR activity in PFC systems, while electricity generation is considered a secondary outcome.

3.9 Reusability and Stability of Electrodes

To evaluate the performance and behaviour of Cu0.5GCN9.5, the transient photocurrent has been measured for five consecutive cycles. Figure 13 **(a)** shows the transient photocurrent of Cu0.5GCN9.5 for five consecutive cycles. As shown in Fig. 13 **(a)**, it can be observed that there are consistent rises and falls of the transient photocurrent during light-on and light-off cycles, which confirms that the Cu0.5GCN9.5 is responsive to light and can generate photoexcited charge carriers under illumination. In the first cycle, the photocathode exhibits the highest photocurrent density with sharp, stable spikes during illumination, indicating efficient charge separation and transport, as well as strong photosensitivity to UVA light, highlighting the proposed PFC's excellent reproducibility in photocurrent generation. However, as the cycles progressed, a gradual decline in photocurrent density was observed in subsequent cycles. Despite this decrease, the consistent shape and response of the photocurrent spikes suggest that the photocathode retains significant activity throughout the experiment, reflecting its relative stability under repeated operation. This phenomenon may be due to photocatalyst degradation over time due to prolonged exposure to UVA and photo-corrosion, and results in electron–hole pairs recombination, leading to a decrease in the number of free charge carriers contributing to the photocurrent (Dimitropoulos et al., 2024). These results emphasize the Cu0.5GCN9.5 photocathode's durability while also identifying areas for improvement. Future studies could focus on enhancing long-term performance by mitigating surface fouling and reducing recombination effects through material modifications.

Fig. 13 **(b)** shows the recyclability evaluation for Cu0.5GCN9.5 photocathode in the degradation of RR120. As shown in **Fig. 13 (b)**, Cu0.5GCN9.5 photocathode showed a gradual decline in photocatalytic efficiency over five cycles, as indicated by the increasing time required for complete degradation of the reactant. After 30 h of operation, a minimal performance loss of approximately 4.04% was observed, likely due to surface deactivation caused by the adsorption of reaction intermediates or by-products blocking active sites. Despite this minor decline, these results indicated that the Cu0.5GCN9.5 photocathode remained highly active throughout the five consecutive cycles, demonstrating its excellent stability during the photocatalytic process

3.10 Proposed Mechanism of Dual Photoelectrodes in PFC System

To further clarify the electron transfer behaviour between the photoanode and photocathode, the

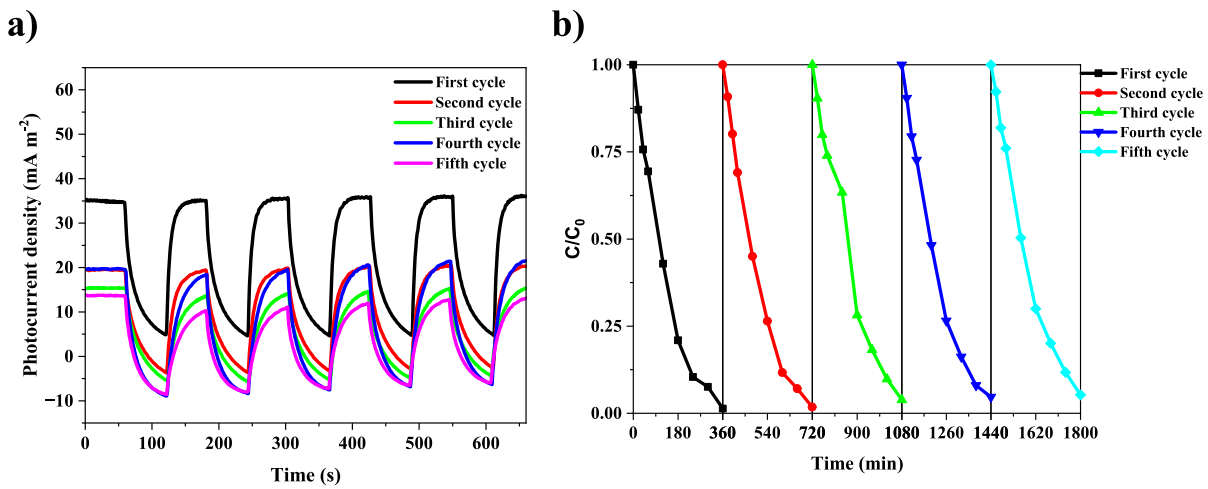

Fig. 13 **(a)** Transient photocurrent and **(b)** recyclability test of Cu0.5GCN9.5 for five consecutive cycles

mechanism of dual photoelectrodes is discussed. In this study, the band edge potentials of the VB and CB of ZnO, nano g-C_3N_4 and CuO were determined by using the following equations (Ong et al., 2019; Serrà et al., 2021):

$$E_{VB} = X - E^e + 0.5E \quad (6)$$

$$E_{CB} = X - E^e - 0.5E_g \quad (7)$$

where X is the electronegativity of the materials, E^e is the energy of free electrons on the hydrogen scale (approximately 4.50 eV) and E_g is the band gap energy of the materials (3.22 eV for ZnO (Ong et al., 2019), 3.08 eV for nano g-C_3N_4 and 1.70 eV for CuO (Allouche et al., 2025)). The X of ZnO, nano g-C_3N_4 and CuO are 5.79, 6.91 and 5.81 eV, respectively (Ong et al., 2019; Praus, 2021; Serrà et al., 2021). According to the formula Eq. (6) and (7), the E_{VB} of ZnO, nano g-C_3N_4 and CuO were calculated as 2.90, 3.95 and 2.16 eV, respectively, while for the E_{CB}, the E_{CB} of ZnO, nano g-C_3N_4 and CuO were calculated as −0.32, 0.87 and 0.46 eV, respectively.

In this work, the Fermi level positions were not experimentally determined but were estimated according to previously published data. According to the literature, the Fermi level of a p-type semiconductor is typically positioned close to its VB, whereas that of an n-type semiconductor lies near the CB (Ahmed et al., 2024; Eroglu & Metin, 2023; Qin et al., 2025b; Ren et al., 2022). For instance, the Fermi level of ZnO is reported to be approximately 0.9 eV below the CB, corresponding to an energy level of around 0.58 eV (Gao et al., 2011; Ong et al., 2019; Zheng et al., 2009). In the case of g-C_3N_4, Li et al., (2016) reported that the Fermi level lies about 1.78 eV above the VB within a band gap of 2.8 eV, indicating that Fermi level is close to the CB. Similarly, (Zehtab Salmasi et al., 2025) found the Fermi level to be 2.25 eV above the VB in a band gap of 2.6 eV, also suggesting a CB-proximal Fermi position. In contrast, CuO, a typical p-type semiconductor, has its Fermi level located approximately 0.2–0.24 eV above the VB (Shao et al., 2011). Therefore, based on these reported values, the E_{VB}, E_{CB}, and Fermi level positions of ZnO, nano g-C_3N_4 and CuO were estimated and illustrated schematically in Fig. 14 to describe the mechanism of dual photoelectrodes configurations PFC system and the possible formation of a heterojunction between the two semiconductors.

In Fig. 14, when the two semiconductors, n-type and p-type, come into contact, the diffusion of electrons and holes occurs, and a p–n junction with a space-charge region is formed at the interfaces, which creates an internal electric field that can direct the electrons to the positive side and holes to the negative side of the internal electric field (Wang et al., 2014; Zeng et al., 2025). Upon light irradiation, both semiconductors absorb photons with energy equal to or greater than the band gaps and generate electron–hole pairs. The photoexcited electrons in the CB of CuO transfer to the CB of g-C_3N_4 through the established p–n junction interface. Conversely, the photogenerated holes in the VB of g-C_3N_4 migrate toward the VB of CuO. This spatial migration of electrons and holes effectively suppresses charge recombination (Wang et al., 2014). As a result, electrons accumulated in g-C_3N_4 actively participate in the ORR, while holes in CuO facilitate the oxidation of pollutants or sacrificial species.

Meanwhile, in Fig. 14 at the photoanode (ZnO), light excitation generates photogenerated holes that oxidise water or organic molecules, releasing electrons into the external circuit. The photoexcited electrons flow spontaneously from the photoanode to the photocathode due to the difference in Fermi level potentials and the internal bias established between the two photoelectrodes (Cai & Feng, 2016). The Fermi level of ZnO photoanode is generally higher than that of the CuO/nano g-C_3N_4 photocathode, and this potential bias leads to spontaneous and sustains the continuous movement of electrons transfer from photoanode to photocathode (Zhong et al., 2025). At the photocathode surface, these electrons participate in the ORR, which serves as the terminal reduction process and driving force for further electron transfer from the photoanode in the PFC system. In addition, the p-n heterojunction between CuO and nano g-C_3N_4 improved charge separation and enhanced ORR activity, minimizing recombination losses and ensuring a steady flow of charge carriers between the photoanode and photocathode (Zhu et al., 2021). Therefore, this dual photoelectrodes configuration PFC system with CuO/nano g-C_3N_4 as photocathode improves both power generation and pollutant degradation efficiency in the photocatalytic fuel cell, and this is

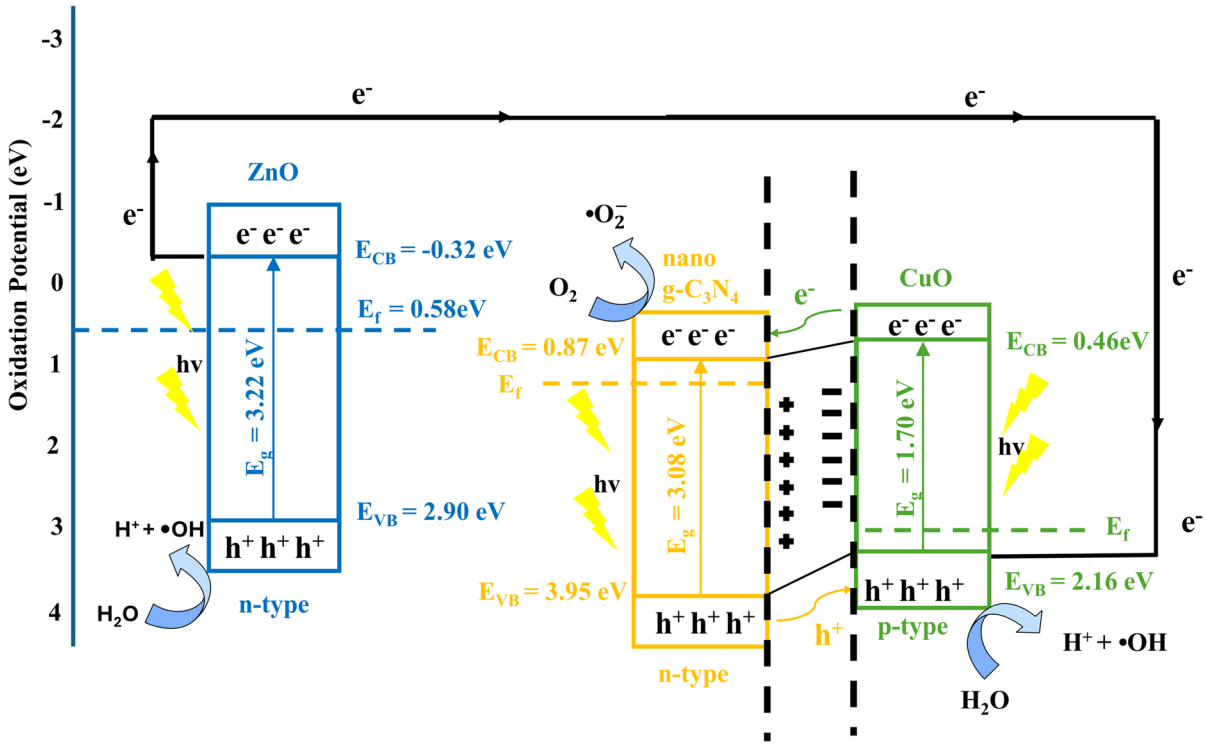

Fig. 14 Schematic diagram for mechanism of dual photoelectrodes configurations in PFC system and the possible formation of a heterojunction between the CuO/nano g-C_3N_4 composite

in good agreement with the results and discussion in Sects. 3.7 and 3.8, which the pollutant degradation and electricity generation for the dual photoelectrodes configuration are superior to the single photoelectrode configurations.

4 Conclusion

In conclusion, a comparative study of the pristine nano g-C_3N_4 and CuO/nano g-C_3N_4 composites loaded on a carbon plate as a cathode for application in PFC was investigated in single and dual photoelectrode configurations, respectively. This study explored the potential of CuO/nano g-C_3N_4 composites, particularly with an optimal CuO loading of 5 wt.% (Cu0.5GCN9.5) — as efficient photo(electro)catalyst materials in dual photoelectrode PFC configurations. Cu0.5GCN9.5 outperformed nano g-C_3N_4, Cu1GCN9 and Cu2GCN8, achieving the overall highest performance with a color removal efficiency of 98% and a power output of 1.35 mW/m^2. Moreover, the dual photoelectrode configuration further enhanced performance, delivering over 13.14% greater decolorization efficiency and 1.58 times more electricity generation than the single electrode configuration for Cu0.5GCN9.5 due to improved electron transfer and reduced charge recombination, thus increasing ORR activity of the cathode as the photo(electro)catalyst was activated by UVA light. Additionally, the CuO/nano g-C_3N_4 composites exhibited higher apparent rate constants (k_{app}) compared to the pristine nano g-C_3N_4, indicating more expeditious RR120 decolourisation efficiency in the PFC system.

Authors Contributions Kang-Zheng Khor: Methodology, Visualization, Writing—original draft preparation. Soon-An Ong: Project administration. Nabilah Aminah Lutpi: Validation. Yunhai Wang: Validation. Jai-Xien OrYang: Validation. Li-Ngee Ho: Supervision, Funding acquisition, Conceptualization, Writing—review & editing.

Funding Open access funding provided by The Ministry of Higher Education Malaysia and Universiti Malaysia Perlis. This research is supported by the Fundamental Research Grant

Scheme (FRGS/1/2022/STG05/UNIMAP/02/1) provided by the Ministry of Higher Education, Malaysia.

Data Availability All data generated or analyzed during this study are included in this published article.

Declarations

Ethical Approval Not applicable.

Consent to Participate Not applicable.

Consent to Publish Not applicable.

Competing interests The authors have no competing interests to declare that are relevant to the content of this article.

References

Ahmed, M. A., Mahmoud, S. A., & Mohamed, A. A. (2024). Unveiling the photocatalytic potential of graphitic carbon nitride (g-C_3N_4): A state-of-the-art review. *RSC Advances, 14*(35), 25629–25662. https://doi.org/10.1039/D4RA04234D

Alemany-Molina, G., Quílez-Bermejo, J., Navlani-García, M., Morallón, E., & Cazorla-Amorós, D. (2022). Efficient and cost-effective ORR electrocatalysts based on low content transition metals highly dispersed on C_3N_4/super-activated carbon composites. *Carbon, 196*, 378–390. https://doi.org/10.1016/j.carbon.2022.05.003

Allouche, N., Boudjema, B., Daira, R., El Sayed, A. M., Abdelkarem, K., Ahmed, I. A., & Shaban, M. (2025). Morphological and optical characterization of spin-coated CuO nanostructured thin films doped with V, Na, Ba, and Er for enhanced CO_2 sensing. *Journal of Materials Research and Technology, 35*, 379–391. https://doi.org/10.1016/j.jmrt.2025.01.048

Almeida, J. S., Batista, W. F. C., Barbosa, L. R. S., Damaceno, F. B., Pires, M. J. M., Mesquita, J. P., Mastelaro, V. R., dos Santos, W. S., Pereira, M. C., & Mourão, H. A. J. L. (2024). Synthesis, structure analysis and Fenton-like catalytic properties of copper-modified graphitic carbon nitride. *Materials Science in Semiconductor Processing, 181*, Article 108642. https://doi.org/10.1016/j.mssp.2024.108642

Anjumol, K. S., Joy, J., Mathew, S. S., Maria, H. J., Spatenka, P., & Thomas, S. (2023). Graphitic carbon nitride-based nanocomposites. *Synthesis, Characterization, and Applications of Graphitic Carbon Nitride: An Emerging Carbonaceous Material*, 59–76. https://doi.org/10.1016/B978-0-12-823038-1.00003-9

Arulkumar, E., & Thanikaikarasan, S. (2024). Structural feature, morphology and optical properties of g-C_3N_4 decorated CuO-Fe_3O_4 nano composite for electrocatalytic and photocatalytic applications. *Diamond and Related Materials, 147*, Article 111294. https://doi.org/10.1016/j.diamond.2024.111294

Arulkumar, E., Thanikaikarasan, S., & Siddhardhan, E. V. (2024). Synthesis and characterization of CuO@NiO/g-C_3N_4 nanocomposite for photocatalytic and electrochemical application. *Results in Chemistry, 7*, Article 101439. https://doi.org/10.1016/j.rechem.2024.101439

Bandaranayake, S., Patnaik, A., Hruska, E., Zhu, Q., Das, S., & Baker, L. R. (2024). Effect of surface electron trapping and small polaron formation on the photocatalytic efficiency of copper(I) and copper(II) oxides. *ACS Applied Materials & Interfaces, 16*(31), 41616–41625. https://doi.org/10.1021/acsami.4c03941

Bentley, C. L., Kang, M., & Unwin, P. R. (2019). Nanoscale surface structure-activity in electrochemistry and electrocatalysis. *Journal of the American Chemical Society, 141*(6), 2179–2193. https://doi.org/10.1021/jacs.8b09828

Blakesley, J. C., & Neher, D. (2011). Relationship between energetic disorder and open-circuit voltage in bulk heterojunction organic solar cells. *Physical Review B, 84*(7), Article 075210. https://doi.org/10.1103/PhysRevB.84.075210

Bojdys, M. J., Müller, J., Antonietti, M., & Thomas, A. (2008). Ionothermal synthesis of crystalline, condensed, graphitic carbon nitride. *Chemistry--A European Journal, 14*(27), 8177–8182. https://doi.org/10.1002/chem.200800190

Cai, Y., & Feng, Y. P. (2016). Review on charge transfer and chemical activity of TiO_2: Mechanism and applications. *Progress in Surface Science, 91*(4), 183–202. https://doi.org/10.1016/j.progsurf.2016.11.001

Chen, P.-W., Li, K., Yu, Y.-X., & Zhang, W.-D. (2017). Cobalt-doped graphitic carbon nitride photocatalysts with high activity for hydrogen evolution. *Applied Surface Science, 392*, 608–615. https://doi.org/10.1016/j.apsusc.2016.09.086

Chubar, N. (2023). XPS determined mechanism of selenite ($HSeO^{3-}$) sorption in absence/presence of sulfate (SO_4^{2-}) on Mg-Al-CO_3 layered double hydroxides (LDHs): Solid phase speciation focus. *Journal of Environmental Chemical Engineering, 11*(3), Article 109669. https://doi.org/10.1016/j.jece.2023.109669

Deng, B., Fu, S., Zhang, Y., Wang, Y., Ma, D., & Dong, S. (2018). Simultaneous pollutant degradation and power generation in visible-light responsive photocatalytic fuel cell with an Ag-TiO_2 loaded photoanode. *Nano-Structures & Nano-Objects, 15*, 167–172. https://doi.org/10.1016/j.nanoso.2017.09.011

Dimitropoulos, M., Aggelopoulos, C. A., Sygellou, L., Tsantis, S. T., Koutsoukos, P. G., & Yannopoulos, S. N. (2024). Unveiling the photocorrosion mechanism of zinc oxide photocatalyst: Interplay between surface corrosion and regeneration. *Journal of Environmental Chemical Engineering, 12*(2), Article 112102. https://doi.org/10.1016/j.jece.2024.112102

Dong, F., Li, Y., Wang, Z., & Ho, W.-K. (2015). Enhanced visible light photocatalytic activity and oxidation ability of porous graphene-like g-C_3N_4 nanosheets via thermal exfoliation. *Applied Surface Science, 358*, 393–403. https://doi.org/10.1016/j.apsusc.2015.04.034

Doren, A., Genet, M. J., & Rouxhet, P. G. (1994). Analysis of poly(ethylene terephthalate) (PET) by XPS. *Surface Science Spectra, 3*(4), 337–341. https://doi.org/10.1116/1.1247762

Eroglu, Z., & Metin, O. (2023). Internal interactions within the complex type-II heterojunction of a graphitic carbon nitride/black phosphorus hybrid decorated with graphene quantum dots: Implications for photooxidation performance. *ACS Applied Nano Materials, 6*(9), 7960–7974. https://doi.org/10.1021/acsanm.3c01187

Fahimirad, B., Asghari, A., & Rajabi, M. (2017). Magnetic graphitic carbon nitride nanoparticles covalently modified with an ethylenediamine for dispersive solid-phase extraction of lead(II) and cadmium(II) prior to their quantitation by FAAS. *Microchimica Acta, 184*(8), 3027–3035. https://doi.org/10.1007/s00604-017-2273-5

Fina, F., Callear, S. K., Carins, G. M., & Irvine, J. T. S. (2015). Structural investigation of graphitic carbon nitride via XRD and neutron diffraction. *Chemistry of Materials, 27*(7), 2612–2618. https://doi.org/10.1021/acs.chemmater.5b00411

Gao, S., Jia, X., Yang, S., Li, Z., & Jiang, K. (2011). Hierarchical Ag/ZnO micro/nanostructure: Green synthesis and enhanced photocatalytic performance. *Journal of Solid State Chemistry, 184*(4), 764–769. https://doi.org/10.1016/j.jssc.2011.01.025

Guadarrama-Pérez, O., Guadarrama-Pérez, V. H., Bustos-Terrones, V., Guillén-Garcés, R. A., Treviño-Quintanilla, L. G., Estrada-Arriaga, E. B., & Moeller-Chávez, G. E. (2024). Bioelectrochemical performance on constructed wetland-microbial fuel cells operated under diffuse and direct solar radiation using root exudates as endogenous substrate to feed an electroactive biofilm. *Electrochimica Acta, 507*, Article 145116. https://doi.org/10.1016/j.electacta.2024.145116

Jeevarathinam, M., & Asharani, I. V. (2024). Synergistic catalytic degradation of crystal violet dye and ciprofloxacin drug using g-C_3N_4/CuO nanocomposites under visible light. *Inorganic Chemistry Communications, 169*, Article 113113. https://doi.org/10.1016/j.inoche.2024.113113

K K, A. V., Dixit, D., Bhattacharya, S., Adhikary, S., & D, G. (2024). A sustainable synthesis of a CuO@C nanocomposite for the remediation of organic dyes in water and its antibacterial properties. *Nano-Structures & Nano-Objects*, *38*, 101147. https://doi.org/10.1016/j.nanoso.2024.101147

Kalisamy, P., Lallimathi, M., Suryamathi, M., Palanivel, B., & Venkatachalam, M. (2020). ZnO-embedded S-doped g-C_3N_4 heterojunction: Mediator-free Z-scheme mechanism for enhanced charge separation and photocatalytic degradation. *RSC Advances, 10*(47), 28365–28375. https://doi.org/10.1039/D0RA04642F

Khampuanbut, A., Kheawhom, S., Kao-ian, W., Limphirat, W., Uyama, H., & Pattananuwat, P. (2024). Unveiling the potential of a g-C_3N_4/BiOBr/$Bi_2O_2CO_3$ ternary heterojunction photocatalyst for rechargeable zinc-air battery: Visible-light-driven photo-assisted charging for bifunctional ORR and OER at the air cathode. *Journal of Power Sources, 612*, 234795. https://doi.org/10.1016/j.jpowsour.2024.234795

Khatun, M., Mitra, P., & Mukherjee, S. (2023). Effect of band gap and particle size on photocatalytic degradation of $NiSnO_3$ nanopowder for some conventional organic dyes. *Hybrid Advances, 4*, Article 100079. https://doi.org/10.1016/j.hybadv.2023.100079

Khor, K. Z., Ho, L. N., Lutpi, N. A., Wang, Y., OrYang, J. X., & Ong, S. A. (2025). Performance of graphitic carbon nitride loaded carbon plate as the photocathode in photocatalytic fuel cell for azo dye degradation and electricity generation. *Springer Proceedings in Physics*, *418 SPPHY*, 206–212. https://doi.org/10.1007/978-981-96-2871-1_29

Kum, J. M., Yoo, S. H., Ali, G., & Cho, S. O. (2013). Photocatalytic hydrogen production over CuO and TiO_2 nanoparticles mixture. *International Journal of Hydrogen Energy, 38*(31), 13541–13546. https://doi.org/10.1016/j.ijhydene.2013.08.004

Lee, S.-L., Ho, L.-N., Ong, S.-A., Wong, Y.-S., Voon, C.-H., Khalik, W. F., Yusoff, N. A., & Nordin, N. (2018). Role of dissolved oxygen on the degradation mechanism of Reactive Green 19 and electricity generation in photocatalytic fuel cell. *Chemosphere, 194*, 675–681. https://doi.org/10.1016/j.chemosphere.2017.11.166

Li, H., Yu, H., Quan, X., Chen, S., & Zhang, Y. (2016). Uncovering the key role of the Fermi level of the electron mediator in a Z-scheme photocatalyst by detecting the charge transfer process of WO_3-metal-gC_3N_4(metal = Cu, Ag, Au). *ACS Applied Materials & Interfaces, 8*(3), 2111–2119. https://doi.org/10.1021/acsami.5b10613

Li, D., Huang, J., Li, R., Chen, P., Chen, D., Cai, M., Liu, H., Feng, Y., Lv, W., & Liu, G. (2021). Synthesis of a carbon dots modified g-C_3N_4/SnO_2 Z-scheme photocatalyst with superior photocatalytic activity for PPCPs degradation under visible light irradiation. *Journal of Hazardous Materials, 401*, Article 123257. https://doi.org/10.1016/j.jhazmat.2020.123257

Li, S., Shi, L., Guo, Y., Wang, J., Liu, D., & Zhao, S. (2024). Selective oxygen reduction reaction: Mechanism understanding, catalyst design and practical application. *Chemical Science, 15*(29), 11188–11228. https://doi.org/10.1039/D4SC02853H

Lie, S., Sandi, M. I., Tay, Y. F., Li, W., Tan, J. M. R., Bishop, D. M., Gunawan, O., & Wong, L. H. (2018). Improving the charge separation and collection at the buffer/absorber interface by double-layered Mn-substituted CZTS. *Solar*

Energy Materials and Solar Cells, 185, 351–358. https://doi.org/10.1016/j.solmat.2018.05.052

Liu, Z., Zhao, Z., Peng, B., Duan, X., & Huang, Y. (2020). Beyond extended surfaces: Understanding the oxygen reduction reaction on nanocatalysts. *Journal of the American Chemical Society, 142*(42), 17812–17827. https://doi.org/10.1021/jacs.0c07696

Liu, G., Zhang, S., Xu, L., Hu, Y., Li, X., Zhang, S., & Zeng, H. (2022). Recent advances of eco-friendly quantum dots light-emitting diodes for display. *Progress in Quantum Electronics, 86*, Article 100415. https://doi.org/10.1016/j.pquantelec.2022.100415

Madima, N., & Raphulu, M. (2025). Platinum group metals-based electrodes for high-performance lithium-oxygen batteries: A mini-review. *Journal of Electroanalytical Chemistry, 976*, Article 118799. https://doi.org/10.1016/j.jelechem.2024.118799

Majdoub, A., Majdoub, M., & Zaitan, H. (2024). G-C3N4/CuO loaded polyester fabric as effective fenton-like dip-catalyst for the oxidation of dyes. *Journal of Water Process Engineering, 60*, Article 105167. https://doi.org/10.1016/j.jwpe.2024.105167

Maluangnont, T., Pulphol, P., Chaithaweep, K., Dabsamut, K., Kobkeatthawin, T., Smith, S. M., Boonchun, A., & Vittayakorn, N. (2023). Alternating current properties of bulk- and nanosheet-graphitic carbon nitride compacts at elevated temperatures. *RSC Advances, 13*(36), 25276–25283. https://doi.org/10.1039/D3RA04520J

Mubeen, K., Irshad, A., Safeen, A., Aziz, U., Safeen, K., Ghani, T., Khan, K., Ali, Z., ul Haq, I., & Shah, A. (2023). Band structure tuning of ZnO/CuO composites for enhanced photocatalytic activity. *Journal of the Saudi Chemical Society, 27*(3), Article 101639. https://doi.org/10.1016/j.jscs.2023.101639

Nasit, M., Vij, A., Kumari, K., Koo, B.-H., Dalela, S., Alvi, P. A., Brajpuriya, R. K., & Kumar, S. (2025). Fabrication and improvement in the electrochemical performance of a 2D g-C_3N_4-based symmetric supercapacitor device. *Journal of Alloys and Compounds, 1013*, Article 178428. https://doi.org/10.1016/j.jallcom.2024.178428

Ong, Y.-P., Ho, L.-N., Ong, S.-A., Banjuraizah, J., Ibrahim, A. H., Lee, S.-L., & Nordin, N. (2019). A synergistic hetero-structured ZnO/$BaTiO_3$ loaded carbon photoanode in photocatalytic fuel cell for degradation of Reactive Red 120 and electricity generation. *Chemosphere, 219*, 277–285. https://doi.org/10.1016/j.chemosphere.2018.12.004

Ong, Y.-P., Ho, L.-N., Ong, S.-A., Banjuraizah, J., Ibrahim, A. H., Lee, S.-L., & Nordin, N. (2020). Comparative study of different polyatomic ions of electrolytes on electricity generation and dye decolourization in photocatalytic fuel cell. *Journal of Water Process Engineering, 37*, Article 101479. https://doi.org/10.1016/j.jwpe.2020.101479

Ong, Y.-P., Ho, L.-N., Ong, S.-A., Banjuraizah, J., Ibrahim, A. H., Thor, S.-H., & Yap, K.-L. (2021). A highly sustainable hydrothermal synthesized MnO_2 as cathodic catalyst in solar photocatalytic fuel cell. *Chemosphere, 263*, Article 128212. https://doi.org/10.1016/j.chemosphere.2020.128212

OrYang, J.-X., Ho, L. N., Lee, C.-C., Khor, K.-Z., & Ong, S.-A. (2025). Graphitic carbon nitride/ zinc oxide hetero-structure photocatalyst for azo dye removal and electricity generation via photocatalytic fuel cell. *International Journal of Nanoelectronics and Materials (IJNeaM), 18*(3), 408–416. https://doi.org/10.58915/ijneam.v18i3.1561

Ouyang, D., Wang, F., Gao, D., Han, W., Hu, X., Qiao, D., & Zhao, X. (2022). Light-driven lignocellulosic biomass conversion for production of energy and chemicals. *iScience, 25*(10), Article 105221. https://doi.org/10.1016/j.isci.2022.105221

Phuong Thi Minh, N., Tokuoka, Y., Imai, W., Hirota, K., Kato, M., & Tsukagoshi, K. (2019). The study of physicochemical properties of antibacterial ZnO powder-impurity doping, elution and catalytic properties (Vol. 60, Issue 2). https://doi.org/10.14988/pa.2019.0000000274

Praus, P. (2021). On electronegativity of graphitic carbon nitride. *Carbon, 172*, 729–732. https://doi.org/10.1016/j.carbon.2020.10.074

Qiao, Q., Xu, Y., Zhong, D., Ke, X., Yang, Y., & Zeng, H. (2024). Visible light responsive photocatalytic fuel cell with Ce-UiO-66/g-C_3N_4/Bi_2WO_6/Ti photoanode for simultaneous degradation of rhodamine B and electricity generation. *Materials Research Bulletin, 179*, Article 112960. https://doi.org/10.1016/j.materresbull.2024.112960

Qin, C., Tian, S., Wang, W., Jiang, Z.-J., & Jiang, Z. (2022). Advances in platinum-based and platinum-free oxygen reduction reaction catalysts for cathodes in direct methanol fuel cells. *Frontiers in Chemistry*. https://doi.org/10.3389/fchem.2022.1073566

Qin, Y., Liu, C., Peng, X., Ma, Z., Li, L., Chen, S., & Zhang, W. (2025). Accelerating charge separation in p-n heterojunction photocathode for photoelectrochemical oxygen reduction and evolution in photo-enhanced zinc-air battery. *Journal of Colloid and Interface Science, 680*, 387–397. https://doi.org/10.1016/j.jcis.2024.11.024

Ren, R., Liu, G., Kim, J. Y., Ardhi, R. E. A., Tran, M. X., Yang, W., & Lee, J. K. (2022). Photoactive g-C_3N_4/CuZIF-67 bifunctional electrocatalyst with staggered p-n heterojunction for rechargeable Zn-air batteries. *Applied Catalysis b: Environmental, 306*, Article 121096. https://doi.org/10.1016/j.apcatb.2022.121096

Riazati, P., & Sheibani, S. (2025). Enhancing photocatalytic water remediation by g-C_3N_4 through controlled CuO content in an S-scheme g-C_3N_4/CuO nanocomposite. *Journal of Alloys and Compounds, 1016*, Article 179008. https://doi.org/10.1016/j.jallcom.2025.179008

Serrà, A., Gómez, E., Michler, J., & Philippe, L. (2021). Facile cost-effective fabrication of Cu@Cu_2O@CuO–microalgae photocatalyst with enhanced visible light degradation of tetracycline. *Chemical Engineering Journal, 413*, Article 127477. https://doi.org/10.1016/j.cej.2020.127477

Shang, W., Wang, H., Yu, W., He, Y., Ma, Y., Li, R., Wu, Z., & Tan, P. (2022). A zinc-air battery capable of working in anaerobic conditions and fast environmental energy harvesting. *Cell Reports Physical Science, 3*(6), Article 100904. https://doi.org/10.1016/j.xcrp.2022.100904

Shao, P., Deng, S., Chen, J., Chen, J., & Xu, N. (2011). Study of field emission, electrical transport, and their correlation of individual single CuO nanowires. *Journal of Applied Physics*. https://doi.org/10.1063/1.3536478

Sharma, K., Raizada, P., Hosseini-Bandegharaei, A., Thakur, P., Kumar, R., Thakur, V. K., Nguyen, V.-H., & Pardeep, S. (2020). Fabrication of efficient CuO/graphitic carbon

nitride based heterogeneous photo-Fenton like catalyst for degradation of 2, 4 dimethyl phenol. *Process Safety and Environmental Protection, 142*, 63–75. https://doi.org/10.1016/j.psep.2020.06.003

Shetty, P. G., & Sudapalli, A. M. (2025). Electrochemical performance of 3D CuO nanoflowers and g-C_3N_4/CuO/PAN composite synthesized by thermal decomposition method. *Diamond and Related Materials, 151*, Article 111782. https://doi.org/10.1016/j.diamond.2024.111782

Sinha, S., Sharma, R., Singh, J., Kumar, S., Singh, R., & Jahan, N. (2025). Experimental and first-principles study of an optimized cylindrical-shaped ZnO/g-C_3N_4 heterojunction for enhanced adsorption and photocatalytic degradation of methylene blue dye. *ACS Omega, 10*(27), 28763–28781. https://doi.org/10.1021/acsomega.4c10430

Sudha, V., Murugadoss, G., & Thangamuthu, R. (2021). Structural and morphological tuning of Cu-based metal oxide nanoparticles by a facile chemical method and highly electrochemical sensing of sulphite. *Scientific Reports, 11*(1), 3413. https://doi.org/10.1038/s41598-021-82741-z

Sunasee, S., Leong, K. H., Wong, K. T., Lee, G., Pichiah, S., Nah, I., Jeon, B.-H., Yoon, Y., & Jang, M. (2019). Sonophotocatalytic degradation of bisphenol A and its intermediates with graphitic carbon nitride. *Environmental Science and Pollution Research, 26*(2), 1082–1093. https://doi.org/10.1007/s11356-017-8729-7

Taghipour, S., Ataie-Ashtiani, B., Hosseini, S. M., & Yeung, K. L. (2022). Graphitic carbon nitride-based composites for photocatalytic abatement of emerging pollutants. In *Nanostructured Carbon Nitrides for Sustainable Energy and Environmental Applications* (pp. 175–214). Elsevier. https://doi.org/10.1016/B978-0-12-823961-2.00001-X

Van Cakenberghe, J., Hiernaut, J. P., Roch, A., & Robert, T. (1981). Exoelectron emission from CuO and NiO films. *Thin Solid Films, 82*(3), 257–272. https://doi.org/10.1016/0040-6090(81)90193-0

Vijayalakshmi, M., Rui, W., Reddy, K. R., Reddy, C. V., & Shim, J. (2024). Hierarchical structures of 2D g-C_3N_4 sheet supported 3D star-shaped flower CuO nanohybrids for improved photoelectrochemical water oxidation and visible light induced photodegradation of antibiotics. *Journal of Environmental Chemical Engineering, 12*(1), Article 111889. https://doi.org/10.1016/j.jece.2024.111889

Wang, H., Zhang, L., Chen, Z., Hu, J., Li, S., Wang, Z., Liu, J., & Wang, X. (2014). Semiconductor heterojunction photocatalysts: Design, construction, and photocatalytic performances. *Chemical Society Reviews, 43*(15), 5234. https://doi.org/10.1039/C4CS00126E

Wang, X., Wang, J., Teng, W., Du, Y., Wu, J., Guo, F., & Chen, B. (2021). Fabrication of highly efficient magnesium silicate and its adsorption behavior towards Cr(VI). *Microporous and Mesoporous Materials, 323*, Article 111196. https://doi.org/10.1016/j.micromeso.2021.111196

Wang, K., Qin, X., Cao, P., Chen, S., Yu, H., & Quan, X. (2023). High-efficiency refractory organic pollutants removal boosted by combining heterogeneous electro-Fenton with electrochemical anodic oxidation over a broad pH range. *Process Safety and Environmental Protection, 177*, 635–642. https://doi.org/10.1016/j.psep.2023.07.042

Wang, R., Zhang, Y., Sun, X., Zhang, Q., Cheng, Z., Xue, W., & Zeng, Q. (2024). Resourceful treatment of complex uranium-organic wastewater by a hybrid tandem photocatalytic fuel cell with SnS_2 nanoplate modified carbon felt cathode. *Journal of Hazardous Materials, 480*, Article 135861. https://doi.org/10.1016/j.jhazmat.2024.135861

Wu, X., Zhao, Q., Zhang, J., Li, S., Liu, H., Liu, K., Li, Y., Kong, D., Sun, H., & Wu, M. (2023). 0D carbon dots intercalated Z-scheme CuO/g-C_3N_4 heterojunction with dual charge transfer pathways for synergetic visible-light-driven photo-Fenton-like catalysis. *Journal of Colloid and Interface Science, 634*, 972–982. https://doi.org/10.1016/j.jcis.2022.12.052

Yang, J., Tian, J., Zhao, Y., Wu, Y., Zhang, Y., Zhao, K., Li, S., Wang, R., Yang, Y., Chen, J., & Liu, Y. (2024). Improving the bioelectrochemical performance of microbial fuel cells using single-atom catalyst nickel combined with graphitic carbon nitride as the cathode catalyst. *International Journal of Hydrogen Energy, 50*, 1257–1266. https://doi.org/10.1016/j.ijhydene.2023.06.259

Yap, K.-L., Ho, L.-N., Ong, S.-A., Guo, K., Oon, Y.-S., Ong, Y.-P., & Thor, S.-H. (2021). Crucial roles of aeration and catalyst on caffeine removal and bioelectricity generation in a double chambered microbial fuel cell integrated electrocatalytic process. *Journal of Environmental Chemical Engineering, 9*(1), Article 104636. https://doi.org/10.1016/j.jece.2020.104636

Yong, Z.-J., Lam, S.-M., Sin, J.-C., Zeng, H., Mohamed, A. R., & Jaffari, Z. H. (2022). Boosting sunlight-powered photocatalytic fuel cell with S-scheme Bi_2WO_6/ZnO nanorod array composite photoanode. *Inorganic Chemistry Communications, 143*, Article 109826. https://doi.org/10.1016/j.inoche.2022.109826

Zandipak, R., Bahramifar, N., Torabi, M., Calero, M., Muñoz-Batista, M. J., & Solís, R. R. (2024). Synergistic effect of graphitic-like carbon nitride and sulfur-based thiazole-linked organic polymer heterostructures for boosting the photocatalytic degradation of pharmaceuticals in water. *Chemical Engineering Journal, 494*, Article 152843. https://doi.org/10.1016/j.cej.2024.152843

Zehtab Salmasi, M., Omidkar, A., Ying, H., & Song, H. (2025). Enhanced phenol degradation in wastewater using non-thermal plasma coupled with NiO/g-C_3N_4 nanocomposite catalyst. *Journal of Environmental Chemical Engineering, 13*(4), Article 117180. https://doi.org/10.1016/j.jece.2025.117180

Zeng, X., Li, B., Liu, R., Li, X., & Zhu, T. (2020). Investigation of promotion effect of Cu doped MnO_2 catalysts on ketone-type VOCs degradation in a one-stage plasma-catalysis system. *Chemical Engineering Journal, 384*, Article 123362. https://doi.org/10.1016/j.cej.2019.123362

Zeng, H., Lam, S.-M., Low, K.-C., Sin, J.-C., Li, H., Lin, H., Huang, L., Huang, H., Xu, L., Lim, J.-W., & Jaffari, Z. H. (2025). Amplified treatment of mariculture effluent and pathogen with synchronously electricity generation in a self-biased photocatalytic fuel cell based on dual photoelectrode. *International Journal of Hydrogen Energy, 137*, 622–635. https://doi.org/10.1016/j.ijhydene.2025.05.148

Zhang, Q., Li, Y., Zhong, J., & Li, J. (2023). Facile construction of CuO/g-C_3N_4 heterojunctions with promoted photocatalytic hydrogen generation behaviors. *Fuel, 353*,

Article 129224. https://doi.org/10.1016/j.fuel.2023.129224

Zhao, Y., Tang, X., Cao, J., Huang, P., Weng, C., & Shen, P. (2022). Balancing the V_{oc}-J_{sc} trade-off in polymer solar cells based on 2-(benzoxazol-2-yl)-acetonitrile end-capped small-molecule acceptors through asymmetry and halogenation of end groups. *Organic Electronics, 102*, Article 106446. https://doi.org/10.1016/j.orgel.2022.106446

Zheng, L., Zheng, Y., Chen, C., Zhan, Y., Lin, X., Zheng, Q., Wei, K., & Zhu, J. (2009). Network structured SnO_2/ZnO heterojunction nanocatalyst with high photocatalytic activity. *Inorganic Chemistry, 48*(5), 1819–1825. https://doi.org/10.1021/ic802293p

Zhong, Y., Yu, M., Dou, R., Yu, X., Tang, J., Li, Q., Wei, L., Wang, K., Zhou, X., Sun, J., & Liu, D. (2025). Enhanced self-biased photocatalytic fuel cell performance by dual-photoelectrode with novel graphene-based substrate for tetracycline photodegradation and electricity production. *Separation and Purification Technology, 357*, Article 130168. https://doi.org/10.1016/j.seppur.2024.130168

Zhu, J.-N., Zhu, X.-Q., Cheng, F.-F., Li, P., Wang, F., Xiao, Y.-W., & Xiong, W.-W. (2019). Preparing copper doped carbon nitride from melamine templated crystalline copper chloride for Fenton-like catalysis. *Applied Catalysis b: Environmental, 256*, Article 117830. https://doi.org/10.1016/j.apcatb.2019.117830

Zhu, L., Luo, J., Dong, G., Lu, Y., Lai, Y., Liu, J., Chen, G., & Zhang, Y. (2021). Enhanced photocatalytic degradation of organic contaminants over a CuO/g-C_3N_4 p–n heterojunction under visible light irradiation. *RSC Advances, 11*(53), 33373–33379. https://doi.org/10.1039/D1RA05329A